

Classification of Synoptic Patterns with Mesoscale Mechanisms for Downslope Windstorms in Korea using the Self-Organizing Map

Yewon Shin¹, Jung-Hoon Kim¹, Hye-Yeong Chun², Wook Jang³, and Seok-Woo Son¹

¹Seoul National University

²Yonsei University

³Korea Meteorological Institute

November 23, 2022

Abstract

Downslope windstorms are responsible for wildfires, wind gusts, and turbulence in the lee side of the Taebaek Mountains, called Yeongdong region (YD) in Korea. We classified the synoptic conditions of the windstorms in the YD using a Self-Organizing Map (SOM). For the windstorm events from 1979 to 2019, sea level pressure anomalies were used to train the SOM. It was found that the synoptic patterns could be classified into three representative types: 1) the south high and north low pattern in spring, 2) the west high and east low pattern in winter, and 3) the strong low-pressure system passing the northern part of Korea. At the 850 hPa level, prevailing southwesterly (northwesterly) flow with warm (cold) advection was dominant in Type 1 (2), and Type 3 presented a well-developed baroclinic system of cyclone. Adiabatic warming by downslope windstorm is the strongest in Type 1, which is likely to have a huge impact on the spread of wildfires. Three mesoscale generation mechanisms were examined under different synoptic patterns. Hydraulic jump theory was dominant for the windstorms in Type 2 due to upstream flows with moderate Froude numbers and inversion layers. The partial reflection of mountain waves was found in all types but more frequent in Type 1 than others. Downslope windstorms with wave breaking at critical levels mostly occurred in Type 1. This objective classification of weather patterns responsible for downslope windstorm in the YD is useful for better prediction and future projection of this event with climate change.

1 **Classification of Synoptic Patterns with Mesoscale Mechanisms for Downslope**
2 **Windstorms in Korea using the Self-Organizing Map**

3
4 **Yewon Shin¹, Jung-Hoon Kim^{1*}, Hye-Yeong Chun², Wook Jang³, and Seok-Woo Son¹**

5
6 ¹School of Earth and Environmental Sciences, Seoul National University, Seoul, South Korea.

7 ²Department of Atmospheric Sciences, Yonsei University, Seoul, South Korea.

8 ³Korea Meteorological Institute, Seoul, South Korea.

9
10 Corresponding author: Prof. Jung-Hoon Kim (jhkim99@snu.ac.kr)

11
12 **Key Points:**

- 13 • Using the Self-Organizing Map algorithm, synoptic patterns for downslope windstorms
14 in Korea are classified into three representative types.
- 15 • Different features for three types are found in the synoptic fields, the Föhn effect, and the
16 characteristics of upstream vertical profiles.
- 17 • Dominant mesoscale mechanisms of the downslope windstorms are different
18 significantly under the three classified synoptic patterns.

19

20

21 Abstract

22 Downslope windstorms are responsible for wildfires, wind gusts, and turbulence in the lee side
23 of the Taebaek Mountains, called Yeongdong region (YD) in Korea. We classified the synoptic
24 conditions of the windstorms in the YD using a Self-Organizing Map (SOM). For the windstorm
25 events from 1979 to 2019, sea level pressure anomalies were used to train the SOM. It was found
26 that the synoptic patterns could be classified into three representative types: 1) the south high and
27 north low pattern in spring, 2) the west high and east low pattern in winter, and 3) the strong
28 low-pressure system passing the northern part of Korea. At the 850 hPa level, prevailing
29 southwesterly (northwesterly) flow with warm (cold) advection was dominant in Type 1 (2), and
30 Type 3 presented a well-developed baroclinic system of cyclone. Adiabatic warming by
31 downslope windstorm is the strongest in Type 1, which is likely to have a huge impact on the
32 spread of wildfires. Three mesoscale generation mechanisms were examined under different
33 synoptic patterns. Hydraulic jump theory was dominant for the windstorms in Type 2 due to
34 upstream flows with moderate Froude numbers and inversion layers. The partial reflection of
35 mountain waves was found in all types but more frequent in Type 1 than others. Downslope
36 windstorms with wave breaking at critical levels mostly occurred in Type 1. This objective
37 classification of weather patterns responsible for downslope windstorm in the YD is useful for
38 better prediction and future projection of this event with climate change.

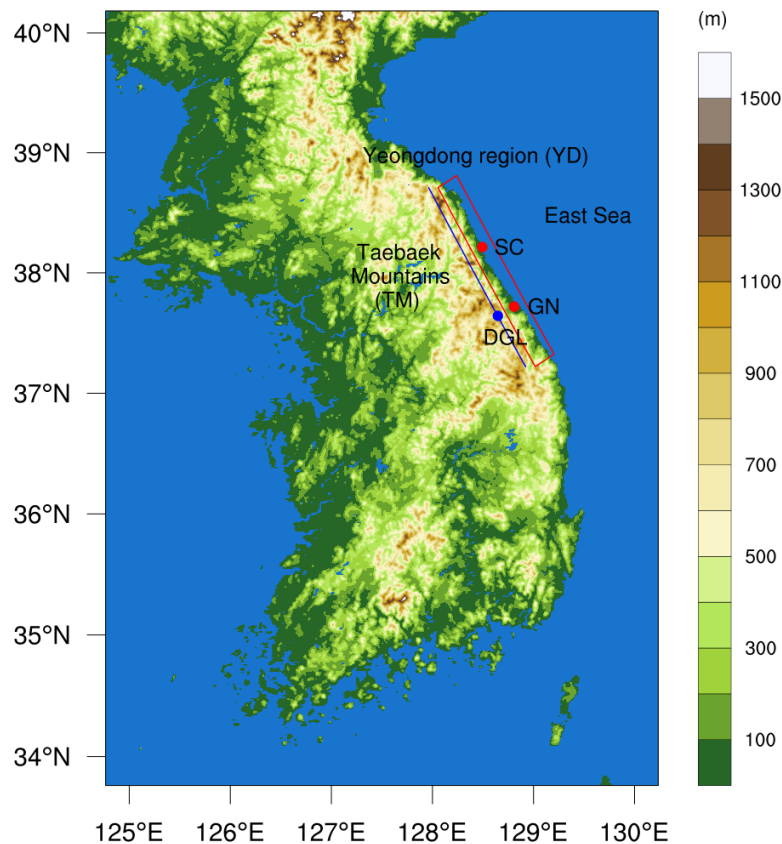
39 1 Introduction

40 Downslope windstorms (DWs), which occur when the atmospheric flow over a mountain
41 accelerates in the mountain's lee, are responsible for wind gusts, turbulence, and rapid spread of
42 wildfires. They are observed in many mountainous regions in the world, including the Rocky
43 Mountains in the United States (Lilly 1978), the Alps in Europe (Hoinka 1985), and the Andes
44 Mountains in South America (Seluchi et al. 2003).

45 Three representative generation mechanisms of the DW have been suggested in the
46 previous studies. Based on the theoretical analysis of Long (1953) on two-dimensional stratified
47 flow over an isolated barrier, Long (1954) proposed the hydraulic jump theory, which suggests
48 that a subcritical upstream flow is changed to a supercritical flow when it goes over a mountain
49 range. An accelerated flow generates severe winds and turbulent jump motion in the lee of a
50 mountain. This transition of flow occurs if the Froude number (Fr) is subcritical but not too
51 small and when the assumed rigid upper surface of the fluid is not too deep compared with the
52 height of the mountain (Long 1954; Houghton and Kasahara 1968). A hydraulic jump occurs
53 even if the rigid lid preventing energy from propagating upward does not exist and the fluid is
54 continuously stratified (Durran 1986). Lin and Wang (1996) divided the flow regimes of a two-
55 dimensional stratified flow over an isolated mountain ridge and reported that a significant lee
56 jump occurred and that severe DW was generated if the Fr was between 0.6 and 1.12. Klemp
57 and Lilly (1975) suggested that vertically propagating mountain waves can be partially reflected
58 at the level of sudden changes in atmospheric stability and vertical wavenumber. The optimal
59 superposition of upward- and downward-propagating waves can amplify the horizontal wind
60 speed near the surface by transporting energy downward. This mechanism, which was developed
61 from the linear theory and the simple mult-layer structure of atmosphere, can be applied in cases
62 when hydraulic jumps cannot explain phenomena due to their restrictive assumptions. Mountain
63 wave breaking at a critical level can cause DW (Clark and Peltier 1984). If upward-propagating
64 stationary waves meet the reversed background zonal wind ($U = 0$) or wave-induced critical

65 level with a local Richardson number (Ri) below 0.25, these waves are not absorbed but instead
 66 strongly reflected. Additionally, if the vertical wavelength is equal to $n + \frac{3}{4}$ ($n = 0, 1, 2, \dots$) of
 67 the critical level height, the constructive resonance of waves can amplify nonlinear wave
 68 breaking above the mountains and can generate intense DWs.

69 In Korea, the Taebaek Mountains (TM) are elongated from north to south in the eastern
 70 side of Korea, and their top heights are approximately $z = 1000\text{--}1500$ m. Figure 1 shows the
 71 topography of Korea, with the locations of the TM and cities on its lee side; this is called the
 72 Yeongdong region (YD). In this region, the lee slope is so steep that DW events frequently occur
 73 in the springtime and the wintertime of Korea and have been responsible for historical wildfires.
 74 DW also caused structural damage, cancellations, and delays of the ski jump and biathlon
 75 competitions on 14–15 Feb 2018 during the 2018 PyeongChang Winter Olympic Games. Many
 76 previous studies have reported that a south high and north low synoptic-scale sea level pressure
 77 (SLP) pattern, accompanied by warm advection and an inversion layer near the top of the
 78 mountains, is often observed when DW occurs in the springtime in the YD (Kim and Chung
 79 2006; Jang and Chun 2010; Cho et al. 2015; Lee et al. 2020). Regarding the generation
 80 mechanisms of DW events in this region, Kim and Chung (2006), and Jang and Chun (2010)
 81 examined the hydraulic jump theory and wave breaking for a DW event on 5 April 2005 when a
 82 historical wildfire occurred. Additionally, Jang and Chun (2008) considered the three
 83 abovementioned mechanisms using 30 years of upstream sounding data (1976–2005) and
 84 revealed that partial reflection, hydraulic jump, and critical level reflection (in that order)
 85 generated the most DW events in the springtime.



87 **Figure 1.** Topography of Korea (shading). Taebaek Mountains (TM) and Yeongdong region
88 (YD) are indicated as a blue line and a red box, respectively. Sokcho (SC) and Gangneung (GN)
89 (two cities in the YD) are depicted as red dots, and Daegwallyeong (DGL) (a town on the TM) is
90 depicted as a blue dot.

91

92 The authors of this study aimed to classify the underlying synoptic SLP patterns
93 responsible for the DWs in the YD in Korea using a self-organizing map (SOM). Though the
94 typical SLP pattern of the DWs is south high and north low in the springtime, there must be other
95 patterns because DW events occur not only in the spring, but also in the late fall and winter (Cho
96 et al. 2015). Several studies have classified weather patterns using clustering algorithms. One
97 method is to characterize the meteorological patterns in the climatological data and investigate
98 the occurrence of extreme weather such as heat waves and heavy rainfall in each pattern (Loikith
99 et al. 2017; Glisan et al. 2016). Cho et al. (2019) classified representative weather patterns in the
100 East Asia region using the k-means clustering algorithm and identified the patterns related to
101 extreme weather in Korea. They also stated that classifying the weather patterns of the specific
102 severe weather phenomena is necessary to gain further insights for better predictions. Jo et al.
103 (2020) classified localized heavy rainfall events in the summertime in South Korea using the k-
104 means clustering and SOM algorithms, and Nguyen-Le and Yamada (2019) also classified
105 synoptic patterns responsible for summertime heavy rainfall over Northwestern Thailand using
106 the two algorithms. Furthermore, many studies have suggested methods to statistically evaluate
107 the forecast skill of patterns recognized by the clustering algorithms, as well as the significant
108 improvements in skill score with this approach (Neal et al. 2016; Ohba et al. 2016; Nguyen-Le
109 and Yamada 2019).

110 In this study, we classified the SLP patterns of DW events using the SOM algorithm and
111 seasonal variability and tropospheric synoptic fields. In addition, we examined the characteristics
112 of the meteorological variables affecting surface environment in the YD and background flows
113 determining the dominant mesoscale mechanisms for the DW events in each pattern. The
114 remainder of this paper is constructed as follows. The data and methods are in Section 2, which
115 explains the definition of the DW events and brief description of the SOM algorithm. Section 3
116 presents the characteristics of the selected DW events. The SLP patterns classified with the
117 SOM, along with corresponding seasonal variability and synoptic-scale composite maps at the
118 850 hPa level, are discussed in Section 4. Section 5 shows the different adiabatic warming effect
119 with temporal changes in the surface temperature in each pattern. In section 6, the dominant
120 mesoscale mechanisms of DWs with analyses of background flows under the different synoptic
121 patterns are addressed. Finally, the conclusion is provided in Section 7.

122 **2 Data and Methods**

123 **2.1 Data**

124 We used the daily maximum instantaneous wind speed obtained from automated surface
125 observing system (ASOS) data measured at Sokcho (SC) and Gangneung (GN) to define the DW
126 events. Hourly surface temperature from the ASOS data measured at GN and Daegwallyeong
127 (DGL) were used to investigate the warming effect of DW. The locations of the surface weather
128 stations at SC, GN, and DGL are indicated in Fig. 1, showing that SC and GN are on the lee side
129 of the TM, and DGL is at the top of the TM and to the west of GN. The SLP and 850 hPa

130 variables (geopotential height, temperature, and horizontal wind speed) obtained from the
131 National Centers for Environmental Prediction–Department of Energy (NCEP–DOE) Reanalysis
132 2 data were used to identify the synoptic-scale patterns of the DWs. This dataset is an improved
133 version of the National Centers for Environmental Prediction–National Center for Atmospheric
134 Research (NCEP–NCAR) reanalysis data with fixed known errors and updated
135 parameterizations. It provides 6 hourly (00, 06, 12, and 18 UTC) global data from 1979 to the
136 present with $2.5^\circ \times 2.5^\circ$ horizontal grid spacing. In addition, the fifth-generation of the ECMWF
137 reanalysis (ERA5) hourly data on pressure levels were used to examine the mesoscale generation
138 mechanisms of the DW events. Their horizontal grid spacing is $0.25^\circ \times 0.25^\circ$, and their vertical
139 layer spacing is 50 hPa for the 750–250 hPa levels and 25 hPa for the 1000–750 and 250–100
140 hPa levels. We used different reanalysis data with different horizontal resolutions for synoptic-
141 scale and mesoscale analyses for two reasons. First, we used the SOM to classify the underlying
142 synoptic-scale patterns with the relatively coarse resolution of reanalysis data because the SOM
143 is sometimes sensitive to local-scale features, especially near mountainous areas. Second, when
144 we further examined the generation mechanisms of the DWs under certain synoptic patterns, it
145 was necessary to look at more detailed mesoscale features from the ERA5 data across the TM.
146 Finally, all datasets mentioned here were used for 41 years from 1979 to 2019.

147 2.2 Identifying Downslope Windstorm Events

148 We defined the DW events when the daily maximum instantaneous wind speed exceeded
149 20 m s^{-1} at SC or GN, which are two cities in the YD (Fig. 1). This value was chosen based on
150 the criterion for issuing the wind advisory by the Korea Meteorological Administration (KMA).
151 Since those data were provided once a day but SLP data were provided four times a day, we
152 divided the event into two separate events in a case that the times when the maximum wind
153 speed was measured at the SC and GN were not close within the same day. To only include
154 windstorms in the YD generated by flows passing over the TM, we excluded cases with wind
155 directions between 0 and 180 degrees, which means that the wind was not from the west. We
156 also excluded cases affected by a typhoon that originally developed from the Northwest Pacific
157 Ocean, because it caused strong gusty winds near surface regardless of DW generation. As a
158 result, we collected 668 cases in total and 600 days with the DW events for 41 years.

159 2.3 Self-Organizing Map (SOM)

160 SOM is a nonlinearly projecting mapping algorithm introduced by Kohonen (1995) that
161 is highly related to classical vector quantization (Kohonen 2013). SOM measures Euclidean
162 distances between each input datum and each initialized node vector. Then, SOM assigns each
163 input datum to the best-matching unit among the nodes, which has the smallest distance from the
164 data. Then, it updates the node vectors of the best-matching and adjacent units toward the input
165 data to minimize the mean distance. By iterating this process and training SOM, it converges to
166 an optimal result. SOM is a kind of unsupervised neural network algorithm, so it can even be
167 used in cases when there is no expected result from input data that is useful for setting up
168 objective classifications or patterns for weather events (Ohba et al. 2016; Loikith et al. 2017;
169 Nguyen-Le and Yamada 2019). SOM usually conducts clustering analysis by dimension
170 reduction, representing high-dimensional input data as a few two-dimensional data. It can
171 additionally be used to extract some predicted features from all data (Liu et al. 2006). SOM is
172 different than other mapping algorithms because SOM preserves topography. In SOM, nodes are

173 arranged in a specified grid on a map. Their topographical relationship is preserved by updating
 174 the vectors of the best-matching and adjacent units together, which are related each other
 175 according to neighborhood functions. Through this process, similar data are associated with
 176 adjacent nodes while dissimilar data are located far away (Kohonen 2013). Therefore, data
 177 become spatially and globally ordered.

178 In this study, SLP anomalies from over 41 years (1979–2019) were used as an input data
 179 to train the SOM. Though many studies have used several meteorological variables together
 180 (multivariate input data) for identifying weather patterns (Ohba et al. 2016; Loikith et al. 2017;
 181 Nguyen-Le and Yamada 2019), we only used SLP anomalies (univariate input data), which show
 182 the representative synoptic-scale patterns for DW in the YD revealed in the previous studies
 183 (Kim and Chung 2006; Jang and Chun 2010; Cho et al. 2015; Lee et al. 2020). The classification
 184 results of multivariate input data (SLP and 850 hPa temperature anomalies) also showed similar
 185 patterns to the test with only SLP anomalies, so we used the classified SLP patterns from the
 186 SOM results with a univariate input and then investigated the composite maps of the synoptic-
 187 scale fields at the 850 hPa level corresponding to each cluster.

188 The domain of the input data was determined as 20–60° N and 100–150° E to focus on the
 189 East Asian region centered on the Korean Peninsula, following the work of Cho et al. (2019),
 190 who showed that this data domain explains better the variance in daily mean surface temperature
 191 driven by synoptic flow in Korea for all seasons compared to results with a larger domain (10–
 192 70° N and 80–160° E). A batch training algorithm was adopted because it is safer and faster than
 193 a stepwise recursive algorithm (Kohonen 2013). The SOM training algorithm contains some
 194 tuning parameters such as lattice structure, map shape, initializing node vector methods, and
 195 neighborhood functions. We used a rectangular lattice of the sheet shape, linear initialization,
 196 and Epanechnikov neighborhood function, as recommended by Liu et al. (2006).

197 The classification results of the SOM are highly dependent on the number of clusters. A
 198 large array with more clusters can show the detailed structures of a pattern, but there should be a
 199 sufficient number of cases (approximately 50) in each cluster for statistical accuracy (Kohonen
 200 2013). To determine the number of clusters while optimally classifying the SLP patterns for the
 201 DW events in the YD, we calculated the ECV (explained cluster variance), which is defined as
 202 (Philipp et al. 2007)

$$203 \quad \text{ECV} = 1 - \frac{\text{WSS}}{\text{TSS}}, \quad (1)$$

204 where WSS is the "within cluster sum of squares of deviations" and TSS is the "total
 205 cluster sum of squares". WSS measures the dissimilarity between data in a cluster, and it is
 206 calculated as (Philipp et al. 2007):

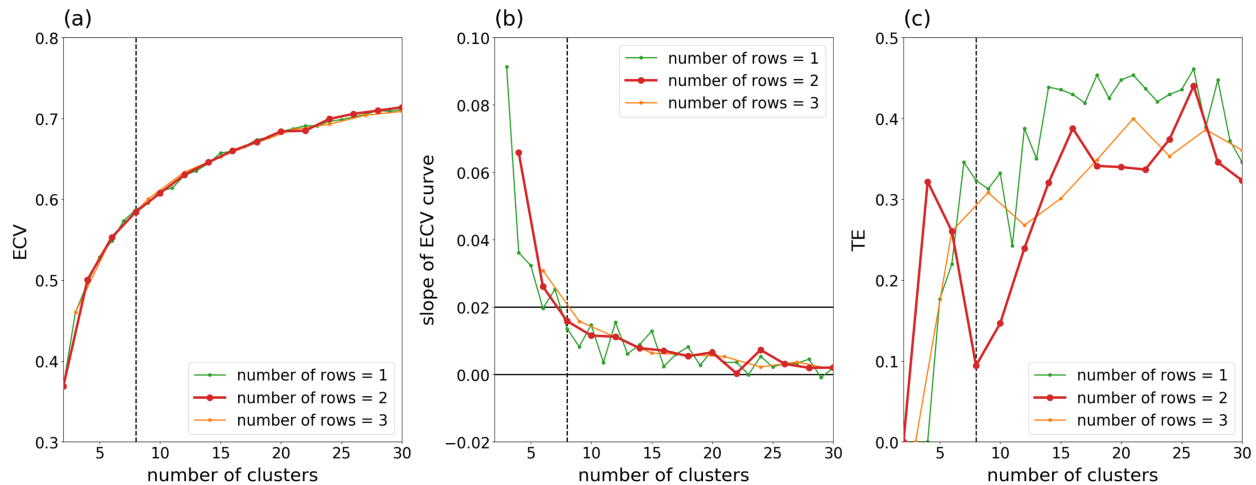
$$207 \quad \text{WSS} = \sum_{j=1}^k \sum_{i \in C_j} D(X_i, \bar{X}_j)^2, \quad (2)$$

208 where k is the number of clusters, C_j is a set of each cluster, X_i is each input datum and
 209 \bar{X}_j is each cluster centroid that can be considered an average of the data in a cluster. Euclidean
 210 distance between each input datum and each cluster centroid is calculated as follows:

$$211 \quad D(X_i, \bar{X}_j) = \left[\sum_{l=1}^m (X_{il} - \bar{X}_{jl})^2 \right]^{1/2}. \quad (3)$$

212 TSS is equal to WSS when $k = 1$ (Philipp et al. 2007). The ECV varies between 0 and 1,
 213 and it is maximized when the centroids fully explain the data in each cluster. Therefore, the ECV

214 measures the ability of cluster centroids to represent and explain the data in each cluster. Figure
 215 2a, b show the ECV and the slope of the ECV curve, respectively. A rapidly increasing ECV was
 216 found to be saturated with an increasing number of clusters. Additionally, we checked the
 217 topographic error (TE) of the SOM. The TE is a ratio of input data in which the first and second
 218 best-matching units (which have the first and second smallest Euclidean distances from the data,
 219 respectively) are not located in the adjacent nodes. If the TE is relatively large, then the SOM
 220 result is not likely to be spatially ordered and optimally classified. In Fig. 2c, the rapidly
 221 increasing TE can be seen as saturated by the large number of clusters, as with ECV but with
 222 more fluctuations, and the TE sometimes has a local minimum in small numbers of clusters, such
 223 as eight with two rows and twelve with three rows. Therefore, we chose the total number of
 224 clusters to be eight (shown as a dashed vertical line in Fig. 2a–c), with two rows and four
 225 columns, when the saturation of ECV begins with the significantly decreasing slope of the ECV
 226 curve below 0.02 (shown as an upper solid horizontal line in Fig. 2b), and the TE has a local
 227 minimum of 0.0943. These choices ensured both the ability to explain the included data within
 228 clusters and the robust topographic relationship of classification result (Kohonen 1995; Kiviluoto
 229 1996), which suggests that the patterns were balanced enough to show a sufficient range of
 230 essential patterns (Nguyen-Le and Yamada 2019).



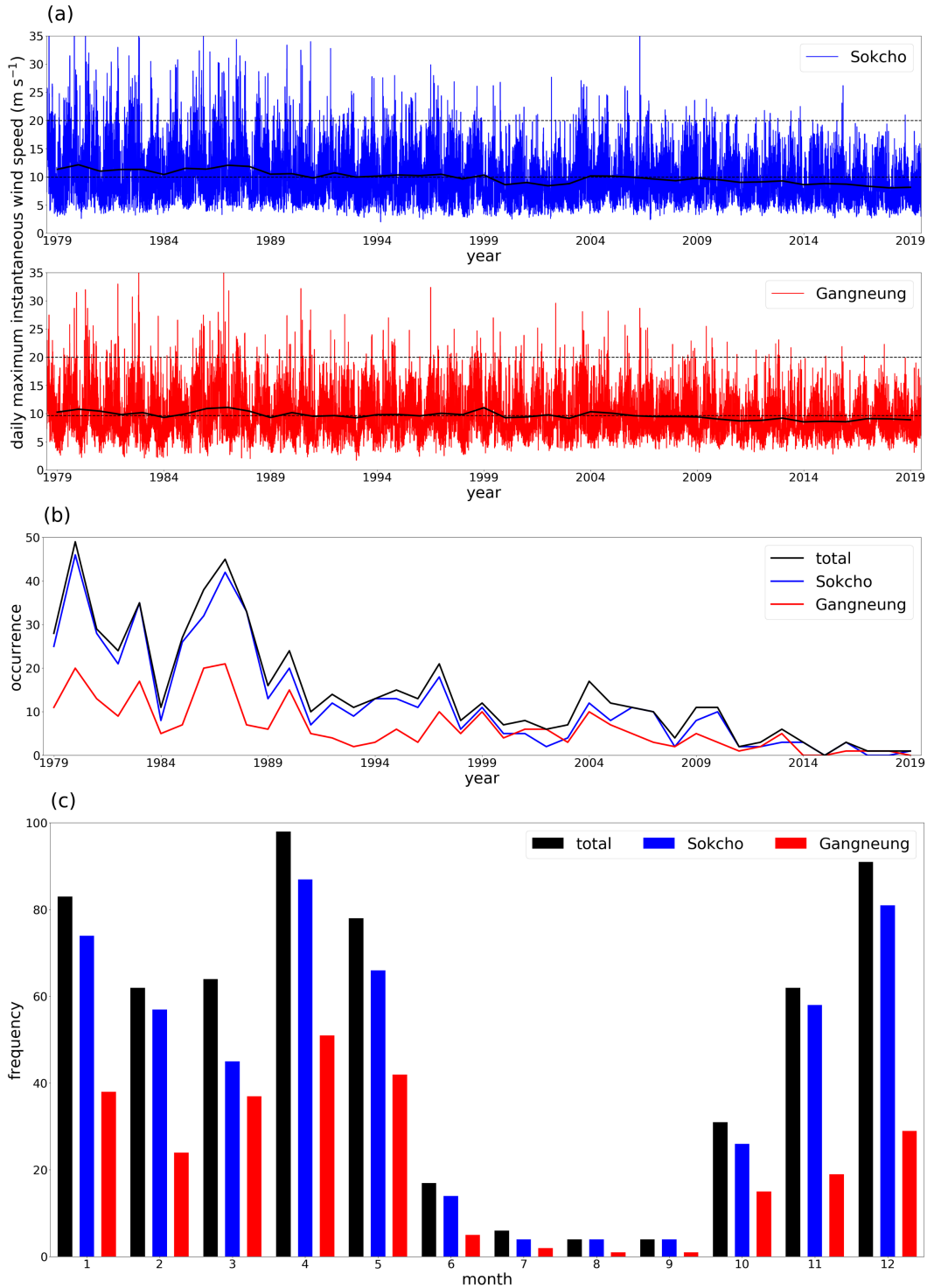
231
 232 **Figure 2.** (a) Explained cluster variance (ECV), (b) the slope of ECV curve, and (c) topographic
 233 error (TE) with the increasing number of clusters for the different number of rows. To determine
 234 the optimal number of clusters, two black horizontal solid lines of zero and the threshold of the
 235 slope (0.02) are drawn in Fig. 2b. The optimal number of clusters, eight, is indicated as a black
 236 vertical dashed line in Fig. 2a–c.

237

238 3 Characteristics of Downslope Windstorm Events

239 This section explains the overall characteristics of DW events for 41 years from 1979 to
 240 2019. Figure 3a shows the time series of the daily maximum instantaneous wind speeds with
 241 their annual mean over the research period at SC and GN on the lee side of the TM. It is likely
 242 that the annual mean speeds decreased over the whole period at both sites, although they slightly
 243 increased in the early 2000s and decreased again in the 2010s. It was also found that the
 244 frequency of DW events had a negative trend as the number of the daily maximum instantaneous
 245 wind speeds exceeding 20 m s^{-1} (upper horizontal black dashed lines in Fig. 3a) gradually

246 decreased. Figure 3b indicates the number of days with DW events in each year. In this figure,
 247 total occurrence means the number of days with DW events in each year at SC or GN. The
 248 frequency of DW events significantly decreased, which is revealed from fewer days of DWs per
 249 year at both sites after 1990 than before 1990. The frequency of DWs slightly increased in the
 250 early 2000s and decreased again in the 2010s (Fig. 3b), which is consistent with the trend of the
 251 daily maximum instantaneous wind speeds in Fig. 3a.



253 **Figure 3.** (a) The time series of the daily maximum instantaneous wind speeds at SC (top) and
 254 GN (bottom). The black solid lines indicate the annual mean daily maximum instantaneous wind
 255 speeds. The upper black dashed lines indicate 20 m s^{-1} (the threshold of DWs in this study), and
 256 the lower ones indicate the mean daily maximum instantaneous wind speed over 41 years. (b)
 257 The number of days with downslope windstorm (DW) events in each year. (c) The monthly
 258 distribution of the whole DW events.

259

260 This long-term DW trend in the YD is similar to those of reports from previous studies.
 261 Decreases in surface wind speeds, namely stilling, have been found to be significant for a few
 262 decades before 2010 on continental areas in the Northern Hemisphere (NH) partly due to
 263 atmospheric circulations (Vautard et al. 2010; Zeng et al. 2019) and/or increase in surface
 264 roughness (Vautard et al. 2010). However, surface wind speeds have recovered over the last
 265 couple decades in global areas (Zeng et al. 2019) including South Korea (Kim and Paik 2015)
 266 due to changes in atmospheric circulations. Though the frequency of DWs decreased in the
 267 2010s, the negative trend before 2000 and the positive trend during the 2000s reported in this
 268 study are consistent with previous studies for wind stilling in NH. Additionally, it has been found
 269 that changes in surface wind speeds are more significant for strong winds (Vautard et al. 2010),
 270 and the annual mean wind speeds at coastal stations in South Korea have been found to more
 271 rapidly decrease before the recovery of stilling than those at inland stations (Kim and Paik 2015).
 272 These facts support the significant decline in instantaneous wind speeds at the two coastal
 273 stations in this study. However, it is not clear whether gusty winds or DW events in the YD will
 274 increase in the future. The overall decreasing trend over the past 41 years does not ensure a
 275 continuous decrease in DW events in the future due to the slight increase in the 2000s, and these
 276 events will be affected by changes in large-scale atmospheric circulations as revealed in previous
 277 studies. Therefore, finding representative patterns for the DW proposed in this study is
 278 necessary to understand underlying large-scale flow patterns with downscaling mesoscale
 279 processes for DW events, which may be eventually useful in projecting these patterns for future
 280 climate scenarios.

281 The time series of the maximum instantaneous wind speeds in Fig. 3a are likely to have
 282 oscillatory patterns with the seasons. To investigate the seasonal variability of DW events, the
 283 monthly frequency of the DW events is shown in Fig. 3c. The monthly distribution of the DW
 284 events shows two peaks in April and December. Consistent with previous studies of DWs in the
 285 YD, they most frequently occurred in the springtime. We found the wintertime to have the
 286 second most frequent DW occurrence and the number of DWs in December to be similar to that
 287 in April. Wintertime DWs in the YD have rarely been addressed in the literature despite their
 288 high frequency, but Cho et al. (2015) mentioned that DWs in the YD also occurred in the fall and
 289 winter from 2005 to 2010. It was expected that the patterns of DWs in the springtime and the
 290 wintertime would be different, which is addressed in Section 4.

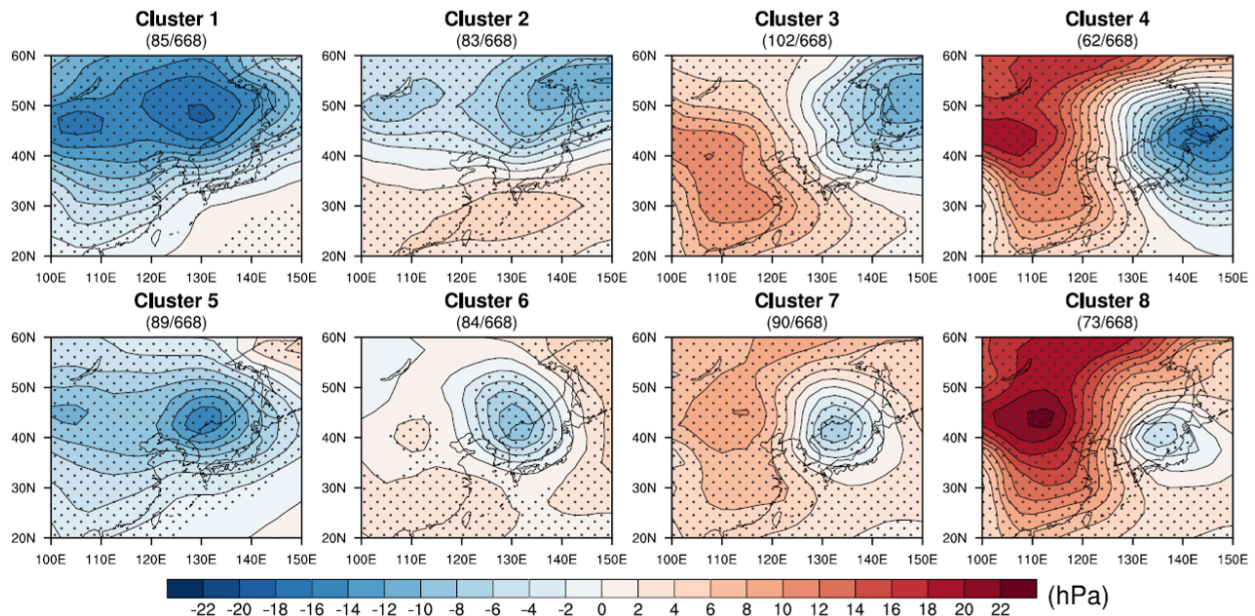
291

292 **4 Classified Synoptic Patterns**

293 **4.1 SLP Patterns**

294 Figure 4 shows the classified synoptic-scale anomalous SLP patterns for the DW events
 295 of the eight clusters based on the SOM. The patterns show the averaged SLP anomalies within

296 each cluster, which are identical to the cluster centroids. The numbers of events in each cluster
 297 displayed at the top of each plot show that the events were evenly distributed to the individual
 298 clusters ranging from 62 to 102, so each cluster centroid is statistically accurate with a sufficient
 299 number of data (Kohonen 2013). We also conducted a Student's t-test to ensure that the
 300 anomalous SLP patterns for the DW events were unique and robust compared with the
 301 climatological SLP anomalies. For all eight SLP patterns, statistically significant areas with p -
 302 values below 0.01 are depicted as black dots in Fig. 4; synoptic-scale high- and low-pressure
 303 systems in all patterns were statistically significant, with the confidence levels higher than 99%.



304

305 **Figure 4.** Synoptic-scale sea level pressure (SLP) anomaly patterns of downslope windstorms
 306 (DWs) for eight clusters classified by the Self-Organizing Map (SOM) averaged within each
 307 cluster; 99% of statistically confident areas below the p -values 0.01 are depicted as black dots.

308

309 The SLP patterns in each cluster were found to be spatially ordered in this node
 310 arrangement. In the patterns on the left side of the node array, high- and low-pressure systems
 311 were found to be in the north and south of the Korean Peninsula, respectively. On the other hand,
 312 in the patterns on the right side of the node array, high- and low-pressure systems were found to
 313 be located in the west and east of the Korean Peninsula, respectively. Additionally, the low-
 314 pressure systems were found to be more localized and located closer to the northern part of the
 315 East Sea of Korea in the patterns at the bottom panel than those at the top panel. All patterns
 316 were found to have very dense isobars across the Korean Peninsula, implying that strong
 317 horizontal pressure gradients are dominant and favorable for strong background winds there.

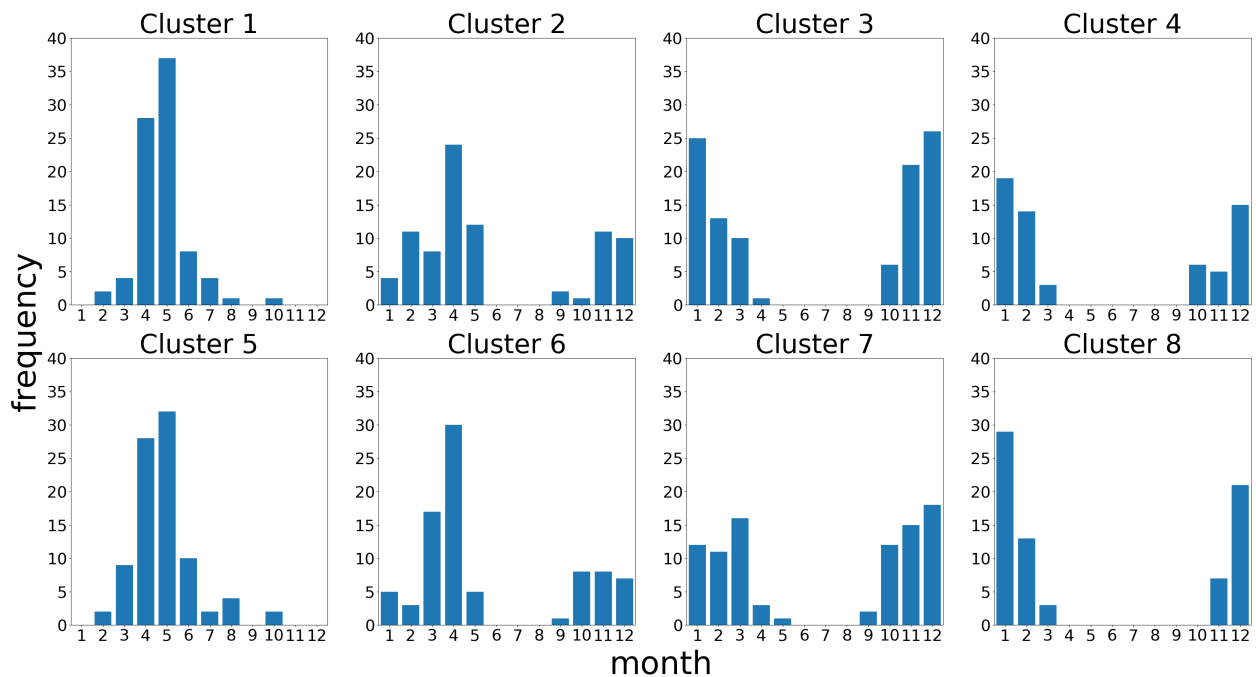
318 Those eight classified patterns could be grouped into three representative types according
 319 to the locations of high- and low-pressure systems relative to the Korean Peninsula. Clusters 1, 2,
 320 and 5 were found to correspond to Type 1, the south high and north low pattern; clusters 3, 4,
 321 and 8 were found to correspond to Type 2, the west high and east low pattern; and clusters 6 and
 322 7 were found to correspond to Type 3, the strong low pressure system passing in the northern
 323 part of Korea. There were differences between clusters in each group, but they showed common
 324 relative locations of high and low SLP anomalies. In Type 1, clusters 1 and 5 were found to show

325 less significant high-pressure systems than cluster 2, but relatively high and low anomalies are in
 326 the south and north of the Korean Peninsula respectively. Similarly, cluster 3 was found to have
 327 a weaker high-pressure system and less dense isobars than clusters 4 and 8 in Type 2, but high
 328 and low anomalies are in the west and east of the Korean Peninsula respectively. Finally, in Type
 329 3, clusters 6 and 7 showed similar patterns to clusters 5 and 8, respectively, due to the
 330 topographical relationship of nodes, but they were only found to have highly significant cyclones
 331 in the northern part of the East Sea of Korea.

332

333 4.2 Monthly Distribution

334 Since synoptic fields in the mid-latitudes are highly dependent on seasons, we
 335 investigated the seasonal variability of each pattern by counting the number of events in each
 336 month. Figure 5 shows monthly frequency bar charts in each cluster. The patterns in the left
 337 panel were found to be more frequent in the springtime from April to May, and those in the right
 338 panel were found to occur more often in the wintertime from December to February. These
 339 results are consistent with the spatial order of clusters and show that the classified SLP patterns
 340 can be divided into springtime and wintertime DWs.



341

342 **Figure 5.** The monthly distribution of downslope windstorm (DW) events in each cluster
 343 classified by SOM.

344

345 The occurrence of Type 1 (clusters 1, 2, and 5 in the left panel in Fig. 5) was found to be
 346 dominant in the springtime. In this pattern, a high-pressure system moves from Central or
 347 Southern China to the Northwest Pacific Ocean and a low-pressure system moving eastward
 348 from Northern China is located in the north or northeast of the Korean Peninsula. Accordingly,
 349 there are dense isobars across the Korean peninsula between the high- and low-pressure systems.
 350 This south high and north low pattern has often been mentioned as a typical synoptic SLP pattern

351 that causes DWs in the YD in previous studies (Kim and Chung 2006; Jang and Chun 2010; Lee
352 et al. 2020).

353 Type 2 (clusters 3, 4, and 8 in the right panel in Fig. 5) was found to mostly occur in the
354 wintertime. In this pattern, a strong high-pressure system (Siberian high) formed by accumulated
355 cold air masses on the Eurasian continent during the winter is extended to eastern China and
356 Korea, and a low-pressure system develops in the East Sea or moves eastward to Hokkaido,
357 Japan (Aleutian low). These systems eventually form dense isobars between the high on the left
358 and the low on the right, consequently providing strong background and gusty surface winds
359 across the Korean Peninsula (Cho et al. 2015).

360 Type 3 (clusters 6 and 7 in the bottom panel in Fig. 5) was observed in both spring and
361 winter. However, cluster 6 was found to most frequently occur in March and April, and cluster 7
362 was found to mostly occur from October to March, reflecting similarity with the spatially close
363 patterns in the SOM node arrangement. Close isobars are formed near the low-pressure system,
364 rather than the relatively weak high-pressure system. This type may have a surface front that can
365 cause strong wind with precipitation in upstream.

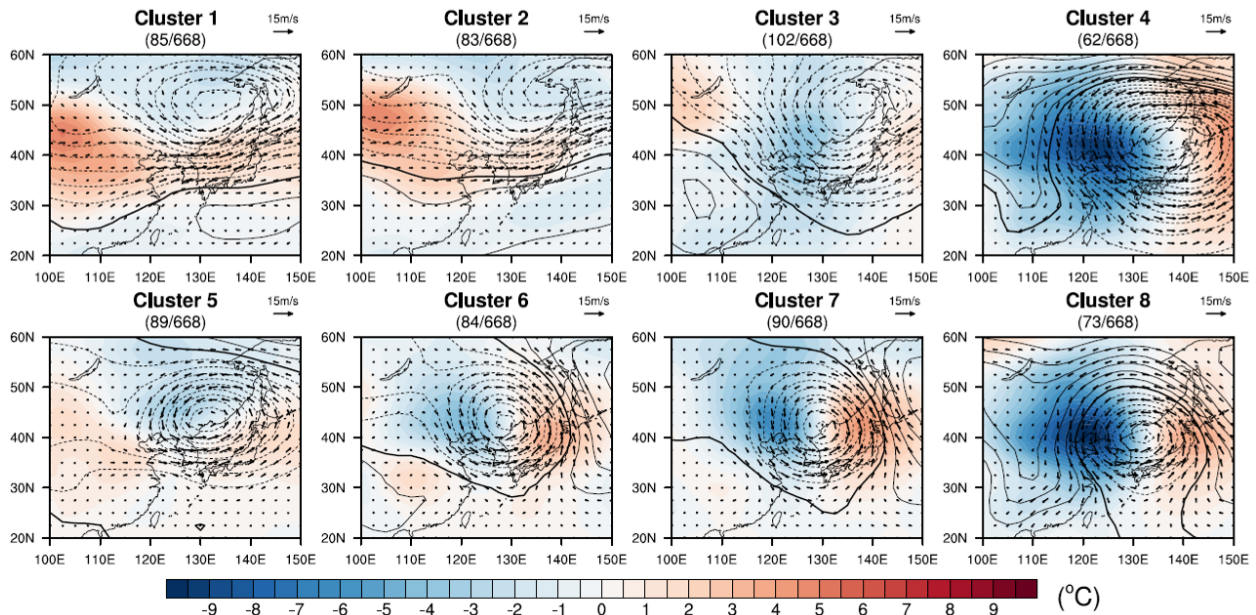
366

367 4.3 850 hPa Synoptic Fields

368 Figure 6 shows the corresponding synoptic fields at the 850 hPa level within each cluster.
369 Anomalies of temperature, geopotential height, and horizontal wind speed were calculated by
370 subtracting monthly averaged data from each set and then by averaging the result within each
371 cluster. This analysis was carried out to compare the fields between clusters with different
372 seasons and to identify relatively warm and cold areas within each cluster. In Type 1 (clusters 1,
373 2, and 5), the prevailing southwesterly flow with warm advection was dominant over the Korean
374 Peninsula. This warm air, which was found to follow the boundary of the high-pressure system
375 from Southern China to the Northwest Pacific Ocean in the spring, flows into Korea with the
376 southwesterly winds. Meanwhile, Type 2 (clusters 3, 4 and 8) shows prevailing northwesterly
377 flow with cold advection over the Korean Peninsula in accordance with the expansion of
378 Siberian high. This cold air mass is from the eastern Eurasian continent, and it moves to Korea
379 when the high-pressure system extends and produces strong northwesterly inflow. Those two
380 patterns can be distinguished from the opposite synoptic thermal characteristics. In Type 3, the
381 areas of cold and warm advection could be identified well in the back and front of the cyclonic
382 anomaly, respectively. The cyclonic circulation was found to be so significant that the low-
383 pressure system centered at the northeastern side of the Korean peninsula could be considered a
384 well-developed, mid-latitude baroclinic cyclone.

385 Type 1 (clusters 1, 2, and 5) has been frequently mentioned as a typical synoptic SLP
386 pattern responsible for the springtime DW events in the YD in Korea in many previous studies.
387 We found that this pattern is accompanied by warm advection at 850 hPa (about $z = 1.5$ km), so
388 an inversion layer is able to be formed near the top of the TM ($z = 1-1.5$ km in Fig. 1) especially
389 when there is surface cooling at night in this pattern. On the other hand, cold advection at 850
390 hPa and the lower troposphere in Type 2 (clusters 3, 4, and 8) can also provide favorable
391 conditions for an inversion layer at the top of Planetary Boundary Layer (PBL) (typically around
392 $z = 1-1.5$ km) when there is surface heating in the daytime. These atmospheric structures with
393 inversion layers at the top of the mountains provide favorable conditions for DWs (Durrán 1990;

394 Wang and Lin 2000; Vosper 2004; Lee and In 2009; Decker and Robinson 2011), which can
 395 promote the optimal superposition of mountain waves that are partially reflected at levels of
 396 sudden change in atmospheric stability (Klemp and Lilly 1975) and hydraulic jump on the lee
 397 slope by enhancing wind speed (Long 1953). More details are provided in Section 6.

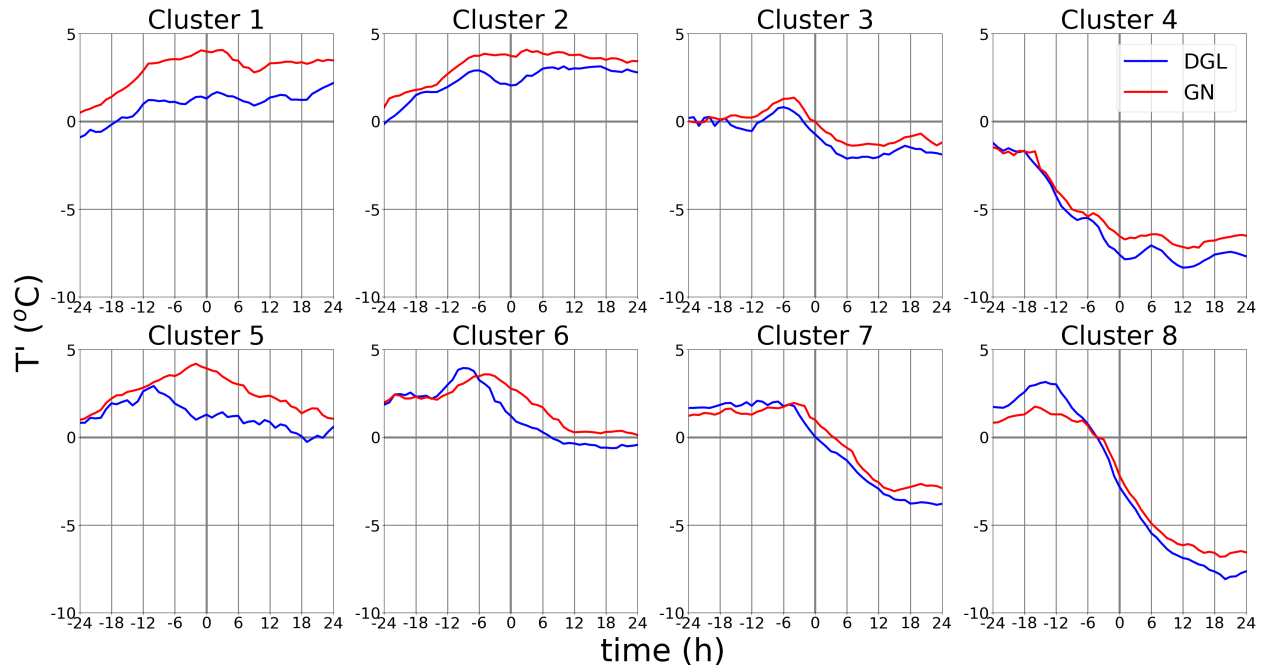


398
 399 **Figure 6.** The 850 hPa geopotential height (solid and dashed lines for positive and negative
 400 values, respectively, in the interval of 10 m), temperature (shading), and horizontal wind (arrow)
 401 anomalies averaged within each cluster.

402

403 5 Adiabatic warming Effect

404 DWs with adiabatic warming on a lee slope cause extremely dry and warm conditions,
 405 thus making them highly related to wildfires, especially in the springtime in the YD in
 406 combination with drought conditions in this area. In order to understand which synoptic pattern
 407 can provide more vulnerable conditions for wildfires via DW events, temporal changes in surface
 408 temperature anomalies were investigated. The surface temperatures measured at GN and DGL
 409 shown in Fig. 1 were considered because GN is a city located on the lee side of the mountains
 410 and DGL is located on a mountain top of the TM at an altitude of approximately 750 m. SC was
 411 not considered here because there were no long-term ASOS data measured at the station located
 412 at the top of the TM to the west of SC, so DW events that occurred when strong winds were only
 413 observed in SC were excluded in this analysis. Here, temperature anomalies were calculated by
 414 subtracting monthly and hourly mean temperatures from measured values to remove both
 415 seasonal and diurnal variations as well as to analyze the impact of DWs. For example, we
 416 subtracted the mean surface temperatures of April 06 UTC measured at each station for 41 years
 417 from all temperature data measured in April 06 UTC. This method was used because there were
 418 no continuously observed surface temperature data over this period with a high enough temporal
 419 resolution to obtain temperature perturbation by Reynolds averaging over a few tens of minutes,
 420 and we wanted to investigate not only the temperature differences between GN and DGL but
 421 also temperature change over time at each station.



422

423 **Figure 7.** Temporal changes in surface temperature anomalies at Gangneung (GN; in the
 424 downstream of Taebaek Mountains; red) and Daegwallyeong (DGL; on Taebaek Mountains;
 425 blue). Data for ± 24 hours around the observed maximum instantaneous wind speeds are shown.

426

427 Figure 7 shows temporal changes in surface temperature anomalies at GN and DGL for
 428 ± 24 hours around the DW event. Note that the maximum daily wind speed was measured at GN
 429 in the middle of each DW event, and temperature anomalies were averaged for the events when
 430 the daily maximum instantaneous wind speed at GN exceeded 20 m s^{-1} in each cluster.
 431 Temperature anomalies at GN at the time of the maximum wind speeds were found to be the
 432 highest in cluster 1 and the lowest in cluster 4, and these values decreased from the left to the
 433 right in the node array. This shows that surface temperature at GN is larger than usual in Type 1
 434 (clusters 1, 2, and 5), and smaller than usual in Type 2 (clusters 3, 4, and 8). In Type 3 (clusters 6
 435 and 7), surface temperature was found to be similar to usual values. Additionally, surface
 436 temperature anomalies increased at both sites as the maximum wind time approached in Type 1,
 437 but they decreased in Type 2. In Type 3, temperature anomalies increased before the maximum
 438 wind time and then increased after. Considering the 850 hPa synoptic field analysis in Section
 439 4.3, it can be estimated that synoptic-scale temperature advection in each pattern contributed to
 440 this result. In Type 1, the increase in surface temperature was found to be larger than usual due to
 441 synoptic warm advection. In Type 2, temperature was found to decrease more than usual due to
 442 synoptic cold advection. In Type 3, temperature was found to increase and then decrease due to
 443 temperature advection around the baroclinic cyclone. Additionally, the increase or decrease in
 444 temperature anomalies was larger when the magnitude of synoptic temperature advection was
 445 greater.

446 In general, surface temperature anomalies were found to be larger in GN than in DGL as
 447 the maximum wind time approachd in all clusters. However, the difference was found to be
 448 much larger in Type 1 near the maximum wind time than any other types. This means that

449 temperature is likely to increase when a flow goes from DGL (mountain top) to GN (lee side).
 450 This increase was found to be the largest in Type 1, implying that temperature increases due to
 451 the adiabatic warming of descending air flow along the DW on the lee slope of the TM (i.e., the
 452 Föhn effect). In summary, the temporal change in surface temperature anomalies at GN and DGL
 453 reflect the synoptic temperature advection at the 850 hPa level, and the larger temperature
 454 anomalies in GN imply that the warming effect due to the downslope wind on the lee side and it
 455 is the strongest in Type 1. This type is a typical pattern of springtime DWs in the YD that has
 456 frequently been mentioned in many previous studies. Additionally, the results of this section
 457 reveal that the warm and dry characteristics of strong winds in this type rapidly promote the
 458 spread of severe wildfires when they occur in this region (Kim and Chung 2006; Jang and Chun
 459 2010).

460 **6 Mesoscale Mechanisms**

461 Under the classified synoptic-scale conditions described in previous sections, we
 462 examined how DW events can be explained by the three representative mesoscale mechanisms:
 463 hydraulic jump theory, partial reflection of mountain waves, and critical level reflection with
 464 wave breaking. We calculated zonal wind speed perpendicular to the mountain range and
 465 atmospheric stability under the corresponding clusters for ± 3 hours around DW events. Then, we
 466 found events that satisfied the conditions of each mechanism and compare their ratio within each
 467 cluster.

468 **6.1 Hydraulic Jump Theory**

469 Hydraulic jump occurs when a subcritical flow in the upstream of a barrier changes to a
 470 supercritical one on the crest or lee slope of a barrier (Long 1954). The critical state is
 471 determined by the Froude number (Fr), which is calculated by the velocity, stability, and depth
 472 of the upstream flow. If Fr is above (or below) a critical value, the flow is supercritical (or
 473 subcritical). Different flow regimes with or without hydraulic jumps in the lee side can be
 474 identified by the following two methods.

475 **6.1.1 Froude Number in a Shallow Water**

476 By considering one-dimensional flow with a free surface or a rigid upper boundary over
 477 an isolated barrier, the motion of a fluid is governed by shallow water equations (Houghton and
 478 Kasahara 1968). In this case, the occurrence of hydraulic jumps is determined by Fr and the
 479 nondimensional height M , defined as follows:

$$480 \quad Fr = \frac{U}{\sqrt{g \frac{\Delta\theta}{\theta_0} h}}, \quad (4)$$

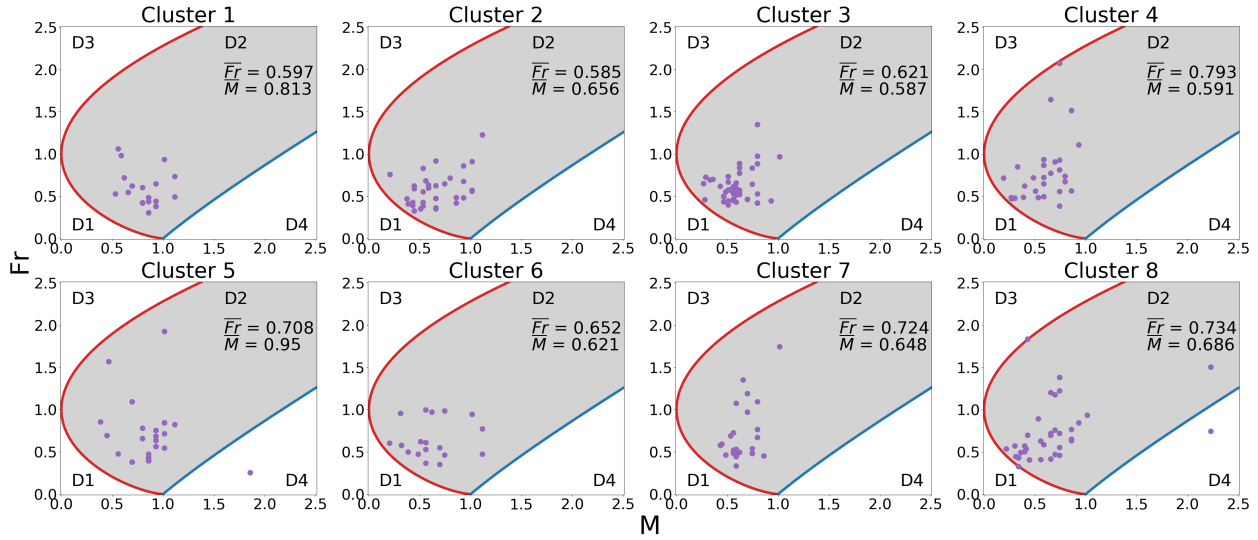
$$481 \quad M = \frac{H}{h}, \quad (5)$$

482 where U is the velocity of fluid, g is gravitational acceleration, θ_0 is potential
 483 temperature of fluid, $\Delta\theta$ is the difference in potential temperature between the two layers, h is
 484 the depth of fluid and H is the mountain height. Here, $H = 1114.543$ m, which was calculated by
 485 averaging the zonal maximum height of the TM (Fig. 1). If Fr in upstream is moderately
 486 subcritical and the flow is not too deep compared to the height of the barrier, the flow becomes
 487 supercritical in the downstream (Long 1954). This supercritical state is achieved if the governing

488 equations of the motion reveal discontinuous jumps on the upper surface, because they cannot
 489 obtain physically meaningful solutions when Fr and M satisfy the following condition:

490
$$M > M_*, \quad (6)$$

491 where $M_* = \frac{Fr^2}{2} - \frac{3}{2}Fr^{2/3} + 1$ is a critical value of M (Houghton and Kasahara 1968).



492

493 **Figure 8.** Fr – M diagrams with points of downslope windstorm (DW) events with inversion
 494 layers in upstream in each cluster. Red and blue lines indicate a critical value of M

495 $\left(M_* = \frac{Fr^2}{2} - \frac{3}{2}Fr^{2/3} + 1\right)$ and Fr of total blocking $\left(Fr = \frac{M-1}{M} \sqrt{\frac{M(M+1)}{2}}\right)$, respectively. The
 496 points in domain 2 (D2 of the shaded areas) indicate hydraulic jumps.

497

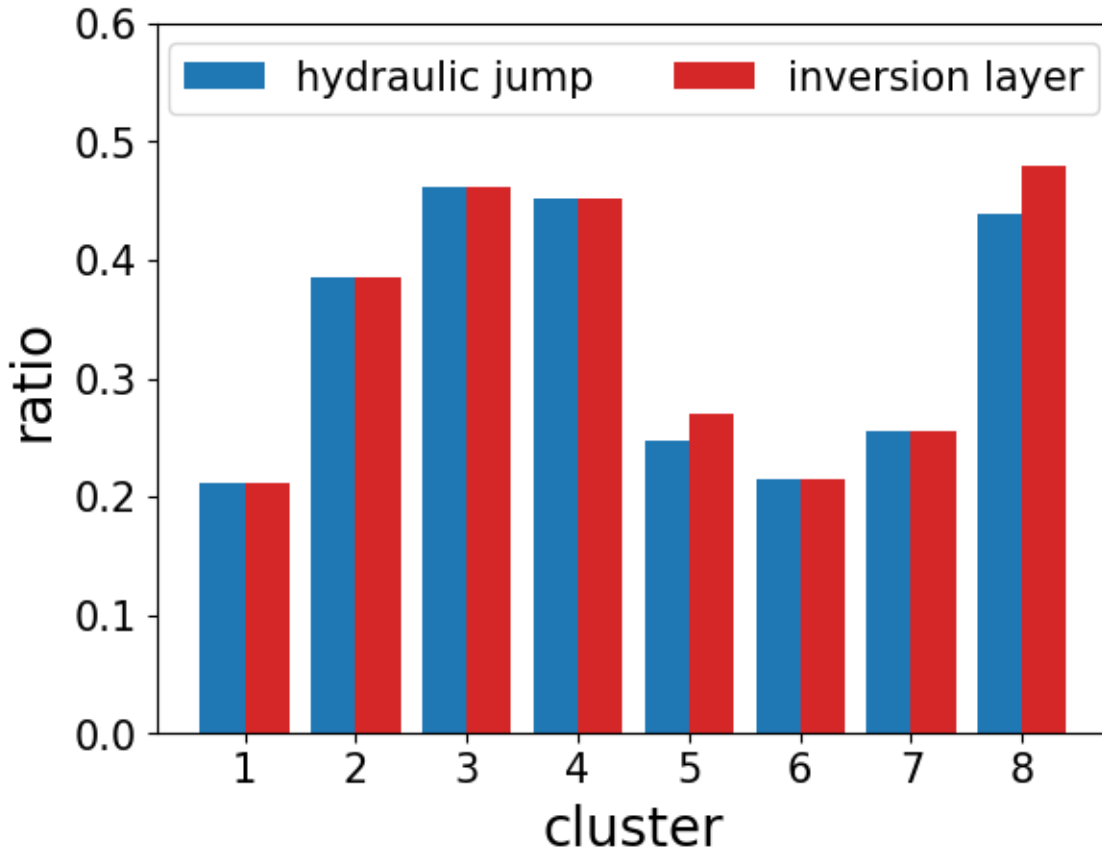
498 Figure 8 shows Fr – M diagrams with a red curve indicating M_* and a blue straight line of

499 total blocking indicating $Fr = \frac{M-1}{M} \sqrt{\frac{M(M+1)}{2}}$ (Houghton and Kasahara 1968) in each cluster. In

500 domains 1 and 3 (D1 and D3, respectively, in Fig. 8), real solutions can exist without
 501 discontinuous jumps because $M < M_*$ (i.e., no hydraulic jump). In domain 4 (D4 in Fig. 8), the
 502 flow is completely blocked by the mountain. In domain 2 (D2 of the shaded areas in Fig. 8), no
 503 solution can exist without a discontinuous jump because $M > M_*$, meaning that the flow must
 504 have discontinuous jumps to satisfy the governing equations. Therefore, the cases in D2 have a
 505 hydraulic jump on the lee side with a transition from subcritical to supercritical flow.

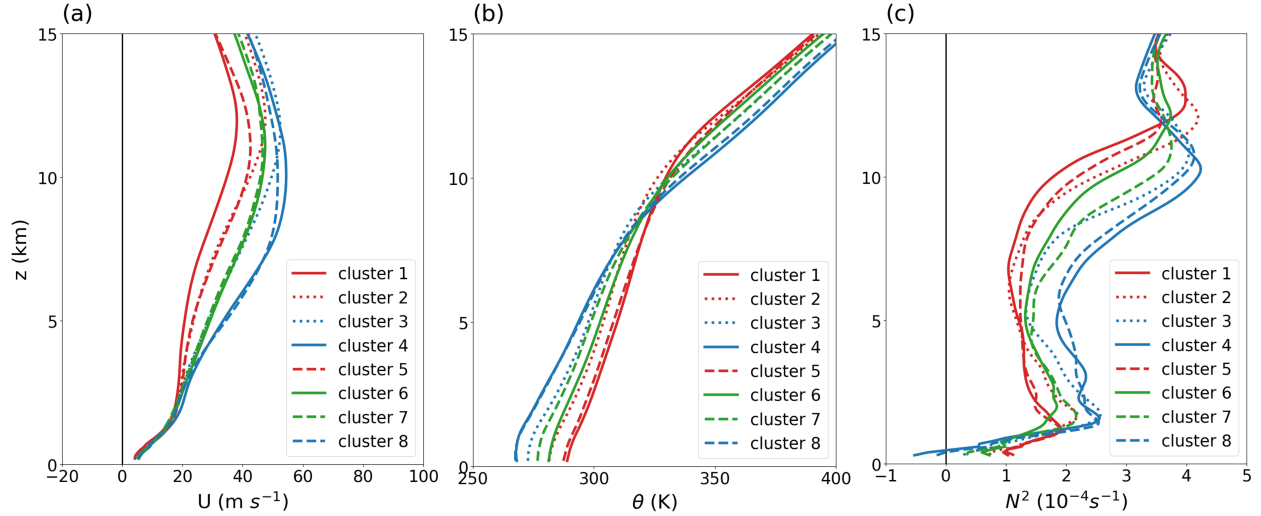
506 Since the flow should have a free surface or a rigid upper boundary to be expressed as
 507 shallow water equations, Fr can only be calculated when there is an inversion layer.
 508 Additionally, hydraulic jumps cannot occur if the depth of the fluid is much larger than the
 509 mountain (Long 1954), so the top height of the inversion layer was set to be below $z = 6000$ m
 510 (which is approximately five times the height of the mountain) in this study. When we calculated
 511 the frequency of the existence of the hydraulic jump and the inversion layer, as shown in Fig. 9,
 512 most cases with inversion layers were found to be in the regime of hydraulic jumps (D2 in Fig.
 513 8), implying that hydraulic jumps mostly occur when there are inversion layers below $z = 6000$

514 m. In addition, Fig. 9 shows that the frequency of hydraulic jump cases was found to be
 515 significantly (more than two times) higher in Type 2 (clusters 3, 4, and 8) than other types.
 516 Therefore, DW events in Type 2 are more likely to be explained by the hydraulic jump theory,
 517 with the more frequent existence of inversion layers acting as a rigid upper bound of flow.



518
 519 **Figure 9.** The ratio of downslope windstorm (DW) events explained by hydraulic jump theory
 520 (blue) and with inversion layers in upstream (red) in each cluster.

521
 522 The results in Figs. 8 and 9 reveal that DW events with hydraulic jumps in wintertime
 523 patterns are more likely to occur under background conditions with frequent inversion layers in
 524 the lower troposphere. In those patterns, the lowest layer of the atmosphere was found to be less
 525 stable, as shown by their nearly neutral potential temperature profiles and lower N^2 values below
 526 $z = 1500$ m (blue lines in Fig. 10b, c), which was possibly due to the mixing in the PBL when
 527 cold advection was dominant just above relatively warm surface with surface heating in the
 528 daytime. The mid-troposphere was more stable and zonal wind is stronger in wintertime patterns
 529 than other patterns, shown as more rapidly increasing wind and potential temperature with height
 530 and higher N^2 values above $z = 1500$ m (blue lines in Fig. 10a–c). Large changes in wind and
 531 static stability between two layers (lower- and mid-troposphere) were found to contribute to the
 532 formation of inversion layers as their interfaces. Nevertheless, this result does not mean that
 533 inversion layers do not exist in the other patterns because the cause of the formation of inversion
 534 layers and their effects on strengthening DWs are different in each pattern.



535

536 **Figure 10.** Vertical profiles of (a) zonal wind speed, (b) potential temperature, and (c) Brunt–
 537 Väisälä frequency averaged in upstream in each cluster. Red, blue, and green lines indicate Type
 538 1 (clusters 1, 2, and 5), 2 (clusters 3, 4, and 8), and 3 (clusters 6 and 7), respectively.

539

540 6.1.2 Froude Number in a Stratified Flow

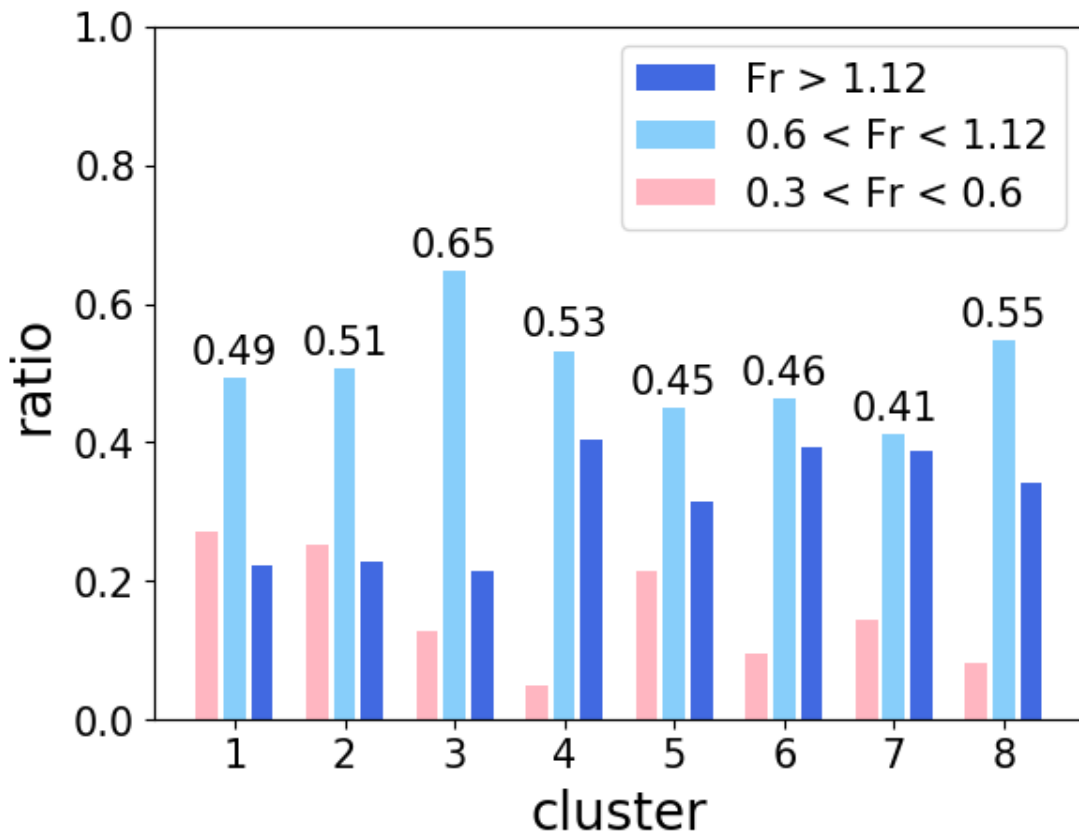
541 The second method to determine the flow regimes related to hydraulic jumps is to
 542 calculate Fr in the upstream by assuming that the flow has uniform wind speed and static
 543 stability with height, as follows:

$$544 \quad Fr = \frac{U}{NH}, \quad (7)$$

545 where U and N are, respectively, the wind speed and Brunt–Väisälä frequency, and
 546 where H is the mountain height. Hydraulic jumps in continuously stratified fluid do not require a
 547 rigid lid or discontinuity in flow (Durrán 1986; Lin and Wang 1996). Durrán (1986) stated that
 548 the transition from subcritical to supercritical flow produces high velocities along the lee slope
 549 by converting potential energy to kinetic energy if there is sufficient acceleration toward a
 550 mountain. Lin and Wang (1996) identified four different regimes for two-dimensional stratified
 551 flow over an isolated mountain range as follows: 1) there is neither downstream wave breaking
 552 nor upstream blocking, so the waves are linear or weakly nonlinear in the absence of lee jumps
 553 ($Fr \geq 1.12$); 2) wave breaking occurs aloft without upstream blocking, and the lee jump
 554 propagates downstream to cause severe DWs ($0.9 \leq Fr \leq 1.12$); 3) wave breaking occurs
 555 earlier than upstream blocking, and the lee jump becomes quasi-stationary, thus causing severe
 556 DWs ($0.6 \leq Fr \leq 0.9$); and 4) upstream blocking occurs earlier than wave breaking and the lee
 557 jump is weak ($0.3 \leq Fr \leq 0.6$). These regimes are consistent with the work of Long (1954),
 558 who found that moderate upstream Fr values in the second and third regimes cause hydraulic
 559 jumps.

560 Here, we calculated Fr by averaging U and N from the surface to 1500 m because in a
 561 real flow they are not uniform with height. We tried using various layer top heights averaging U
 562 and N to test its sensitivity to Fr , and we found systematic increases in Fr and height, possibly
 563 due to the increasing U with height in the mid-latitudes. Finally, we chose 1500 m, because it is

564 slightly above the top of TM, so the airflow below this level is mostly affected by the mountains.
 565 This value was also used in previous studies on DW events in the YD (Kim and Chung 2006;
 566 Jang and Chun 2008). Note that here, Fr was calculated for all events including those without
 567 inversion layers, unlike the method used in Section 6.1.1. Then, we investigated the ratio of the
 568 events in each flow regime following Lin and Wang (1996) explained above: 1) the jump is too
 569 weak to generate the severe DWs in the downstream ($0.3 \leq Fr \leq 0.6$); 2) significant hydraulic
 570 jumps cause severe DWs ($0.6 \leq Fr \leq 1.12$); and 3) flow is so linear that it does not produce
 571 hydraulic jumps ($Fr \geq 1.12$). Here, the second ($0.9 \leq Fr \leq 1.12$) and third ($0.6 \leq Fr \leq 0.9$)
 572 flow regimes of Lin and Wang (1996) were combined into one because both regimes commonly
 573 have hydraulic jumps with severe DWs in the lee side.



574

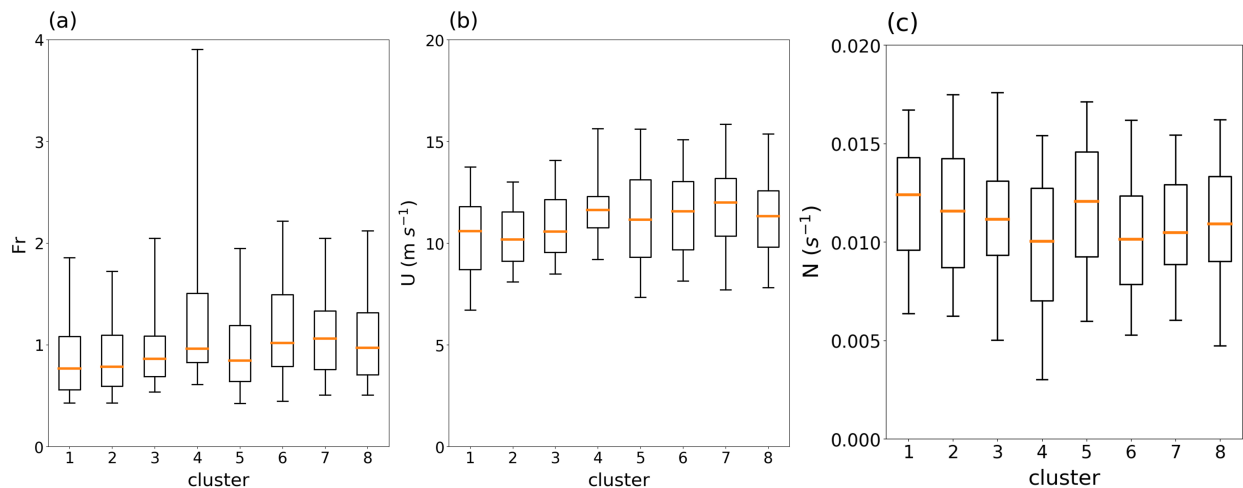
575 **Figure 11.** The ratio of downslope windstorm (DW) events in highly nonlinear flow regime with
 576 weak jumps ($Fr \geq 1.12$; pink bars), moderate flow regime with significant lee jumps and severe
 577 winds ($0.6 \leq Fr \leq 1.12$; skyblue bars with numbers), and linear flow regime without lee jumps
 578 ($0.3 \leq Fr \leq 0.6$; blue bars).

579

580 Figure 11 shows the ratio of the cases for three different flow regimes in each cluster.
 581 The ratios of the strong hydraulic jump regime ($0.6 \leq Fr \leq 1.12$; skyblue bars in Fig. 11) are
 582 0.4–0.7 in the clusters, which are slightly higher than 0.39, the ratio of hydraulic jumps to
 583 springtime DWs in Jang and Chun (2008). In particular, clusters 3, 4, and 8 in Type 2 showed the
 584 first (69%), second (62%), and fourth highest (50%) ratio of lee jumps, respectively. This is
 585 consistent with the results shown in Figs. 9 and 10, where it can be seen that the Type 2 has more

586 frequent strong hydraulic jump regimes with moderate Fr values. The frequencies in the linear
 587 flow regime ($Fr \geq 1.12$; blue bars in Fig. 11) were also relatively larger in Types 2 and 3
 588 compared to Type 1, meaning that the inflow (and thus downstream flow) was already
 589 supercritical. The frequencies in the weak jump regime ($0.3 \leq Fr \leq 0.6$; pink bars in Fig. 11) in
 590 Type 1 (clusters 1, 2, and 5) were found to be significantly larger than those in other types.
 591 Under the Type 1 pattern of the south high- and north low-pressure systems around Korea in the
 592 springtime, Fr is not large enough to produce significant lee jumps and severe DWs, implying
 593 that there must be other mechanisms related to the high frequency of DWs in the springtime;
 594 these are examined in the following sections.

595 In summary, the significant hydraulic jumps responsible for severe winds on the lee slope
 596 were found to be more frequent in wintertime patterns than in the other patterns due to the more
 597 frequent occurrence of moderate Fr values. Type 1 was found to have small numbers of
 598 hydraulic jump cases due to large number of cases in a weak jump regime, and Type 3 was
 599 because it was found to have both many large and small Fr cases. These results can be explained
 600 by mean vertical profiles of zonal wind speed, potential temperature and Brunt–Väisälä
 601 frequency in Fig. 10 and by box plots of Fr , U , and N in Fig. 12. Zonal wind was found to be
 602 stronger in all levels in the wintertime patterns than the others (Fig. 10a), meaning that U is
 603 higher in this pattern (Fig. 12b). Lower troposphere below 1500 m was found to be less stable in
 604 the wintertime patterns (Fig. 10b, c), so N is smaller in this pattern than others (Fig. 12c).
 605 Therefore, in wintertime patterns, the higher Fr (Fig. 12a), which is resulted in slightly higher U
 606 (Fig. 12b) and much lower N (Fig. 12c), causes more events to be included in the strong
 607 hydraulic jump regimes.



608

609 **Figure 12.** Box plots of (a) Fr , (b) U , and (c) N in each cluster. Orange solid lines indicate the
 610 medians. Boxes include from the 1st to 3rd quartiles, and whiskers indicate the 5th and 95th
 611 percentiles.

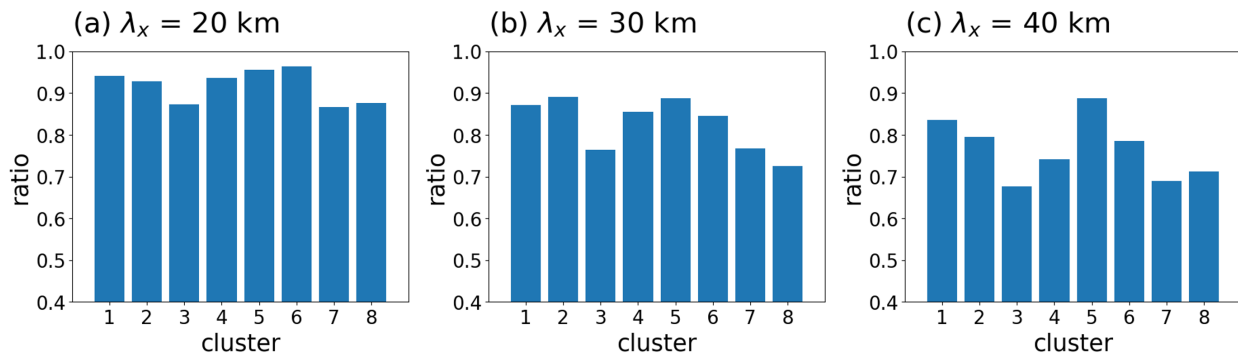
612 6.2 Partial Reflection of Mountain Waves

613 Klemp and Lilly (1975) suggested that upward-propagating mountain waves can be
 614 partially reflected if the Scorer parameter rapidly changes due to variations in wind and thermal
 615 stability. Then, the optimal superposition of upward- and downward-propagating waves can
 616 transport the reflected energy and amplify surface wind speed downstream of mountains. This

617 generation mechanism of DW is called the partial reflection of mountain waves. Though this is
 618 drawn by a linear multi-layer model with idealized vertical profiles where wind and stability are
 619 constant in each layer, we calculated the Scorer parameter l of vertically varying wind and
 620 stability to identify the vertical structure of mountain waves in real cases, as illustrated below:

$$621 \quad l^2 = \frac{N^2}{U^2} - \frac{1}{U} \frac{d^2 U}{dz^2}, \quad (8)$$

622 where U and N are zonal wind speed and Brunt–Väisälä frequency at each vertical level,
 623 respectively (Scorer 1949). The square of the Scorer parameter is the sum of the square of
 624 horizontal and vertical wavenumber (k and m , respectively), and we used this value to obtain the
 625 square of the vertical wavenumber ($m^2 = l^2 - k^2$) at each level. In this calculation, we assumed
 626 that the horizontal wavelengths could vary from 5 to 50 km based on previous studies on DW
 627 (Jang and Chun 2008; 2010) and mountain wave-induced turbulence (Kim and Chun 2010) in
 628 this region, which showed that the dominant horizontal wavelengths of the mountain waves were
 629 approximately 10–25 km. Finally, following the work of Jang and Chun (2008; 2010), whether a
 630 level of trapped mountain waves with negative vertical wavenumber ($m^2 < 0$) exists in each
 631 case was examined. Here, the partial reflection mechanism was investigated by examining the
 632 existence of the reflection of vertically propagating mountain waves (i.e., $m^2 < 0$). Additional
 633 conditions for the optimal superposition of waves generating severe DWs were not tested
 634 because 1) the real vertical structures of the atmosphere are too different from idealized ones for
 635 comparison to the multi-layer model generating partial reflection and resonance of waves, and 2)
 636 vertical wavelengths varying with heights become infinite near the levels of zero vertical
 637 wavenumbers, which makes it hard to identify the optimal conditions for the resonance of waves.
 638 Note that reflection levels were found above $z = 2000$ m because the variation in the wind
 639 curvature term in the Scorer parameter was found to be too large due to the wind shear in the
 640 lower troposphere; consequently, no waves can grow above this layer.



641
 642 **Figure 13.** The ratio of downslope windstorm (DW) events generated by partial reflection of
 643 mountain waves with horizontal wavelengths of (a) 20 km, (b) 30 km, and (c) 40 km in each
 644 cluster.

645 Figure 13 shows the ratio of cases with reflected mountain waves in each cluster when
 646 horizontal wavelengths were set to 20, 30, and 40 km (Fig. 13a, b, c, respectively). DW events in
 647 springtime patterns are more often generated by the reflection of mountain waves than those in
 648 wintertime patterns. This is because clusters in Type 1 (frequent in the spring) have larger ratios
 649 than those in Type 2 (frequent in the winter); additionally, cluster 6 (relatively frequent in the
 650 spring) was found to have a larger ratio than cluster 7 (relatively frequent the in winter) in Type
 651 3. In addition, the difference in the ratios between springtime and wintertime patterns was found

652 to become larger as the horizontal wavelengths became longer. This implies that in springtime
 653 patterns, there are more cases related to the reflection of short-to-long mountain waves and,
 654 consequently, more energy transported to the surface. Meanwhile large-scale mountain waves in
 655 wintertime patterns can propagate to the upper atmosphere and remain unfiltered in the upper-
 656 level (Kim and Chun 2010) in many cases due to the large vertical wavenumber of the large
 657 horizontal wavelength without their energy being transported to the surface.

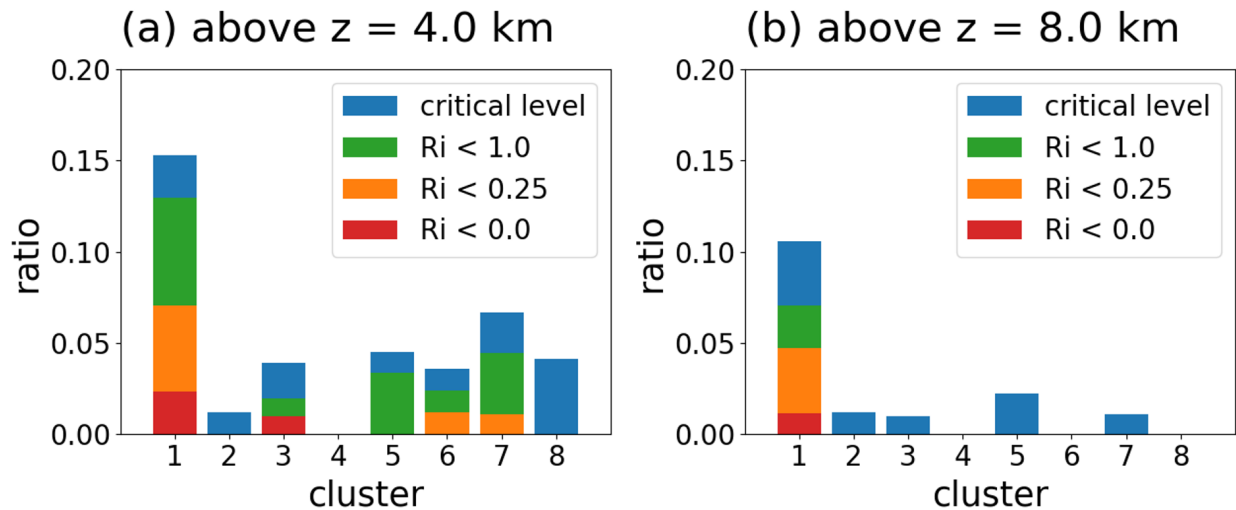
658 In Fig. 10a, mean wind speed can be seen to be relatively weaker in all levels in
 659 springtime patterns than wintertime patterns, but stability in the mid-troposphere can be seen to
 660 be much lower in springtime patterns than wintertime patterns. When considering the first term
 661 on the right hand side of Eq. 8, significant reduction of stability, especially in the mid-
 662 troposphere in springtime patterns, is likely related to conditions for the partial reflection of
 663 waves and responsible for trapped lee waves associated with DWs (Kim and Chun 2010).
 664 Nevertheless, the overall ratios of reflected waves were found to be 0.8–0.9, suggesting that the
 665 partial reflection of mountain waves occur in most DW cases, which is consistent with the work
 666 of Jang and Chun (2008) showing that 84% of springtime DWs were related to the partial
 667 reflection of mountain waves. This is probably because levels of sudden change in static stability
 668 or wind curvature have existed in most cases. Static stability in the atmosphere rapidly changes
 669 near an inversion layer, and wind curvature increases strongly below a jet stream. These
 670 atmospheric structures are likely to be common in many DW cases, so the reflection of mountain
 671 waves and downward energy transport occur in most DW cases.

672 6.3 Critical Level Reflection with Wave Breaking

673 Clark and Peltier (1984) suggested that vertically propagating mountain waves are
 674 reflected in the presence of a background or wave-induced critical level with a reversal of wind
 675 direction and a Richardson number (Ri) smaller than 0.25 near the critical level. If the ratio of
 676 the critical level height to the vertical wavelength is $n + \frac{3}{4}$ ($n = 0, 1, 2, \dots$), the constructive
 677 superposition of incident and reflected waves can cause resonantly amplified wind speed near the
 678 surface by increasing surface wave drags. We determined DW events with wave breaking at
 679 critical levels via the following procedures. First, the existence of reversed flow was examined.
 680 The cases with easterly flow at the points above the lee sides of mountains and westerly flow
 681 below for ± 3 hours around the DW events were identified as critical levels for stationary
 682 mountain waves. Finding the local regions of flow reversal with height indicated the wave
 683 breaking of vertically propagating stationary mountain waves. Second, the Ri near the critical
 684 level (i.e., local region of wind reversal) was considered. Though the critical level reflection was
 685 found to occur when $Ri < 0.25$ in a stably stratified flow (Howard 1961; Miles 1961), we
 686 identified the cases with $Ri < 1$ near the reversed flow as the critical level reflection, because in
 687 the three-dimensional flow of real atmosphere (i.e., nonlinear flow), the stable condition of flow
 688 is often violated even when $Ri < 1$ (Abarbanel et al. 1984; 1986; Miles 1986).

689 Figure 14a, b shows the ratio of DW events with a critical level or reflection above $z =$
 690 4000 and 8000 m in each cluster, respectively. The overall ratio can be seen to have been very
 691 small, approximately 10%, because the flow in the upper-troposphere was usually strong
 692 westerly in the mid-latitudes, and the ERA5 data do not have a good enough vertical and
 693 horizontal resolution to fully resolve vertically propagating mesoscale mountain waves and their
 694 subsequent self-induced critical levels by breaking large amplitude waves. This result is similar

695 to that of Jang and Chun (2008), who showed that only about 5% of springtime DW events in
 696 this region had a critical level by examining upstream sounding data. Comparing the ratios
 697 between clusters revealed that critical levels are produced and critical level reflections occur
 698 ($Ri < 1$) most frequently in cluster 1 (Type 1), which is a south high and north low pattern in the
 699 spring. Though some cases in clusters 3, 6, 7, and 8 were found to have critical levels, there were
 700 no critical levels in the upper atmosphere in most cases. Most critical levels in cluster 1 were
 701 found to exist above 8000 m. Additionally, the ratio of critical level reflection ($Ri < 1$) was
 702 found to be the highest in cluster 1. In summary, both the existence of critical levels in the upper
 703 layer and the occurrence of critical level reflection due to instability were found to be the most
 704 frequent in the south high and north low pattern in cluster 1, so DWs generated by critical level
 705 reflection and wave breaking are most likely to be included in this pattern. This is partly because
 706 upper-level winds that are weaker in springtime patterns (red lines in Fig. 10a) than in wintertime
 707 patterns (blue lines in Fig. 10a) create better conditions for the critical level of high amplitude
 708 vertically propagating mountain waves, and their subsequent breakdowns can provide more
 709 chances to have small but positive Ri values conducive to shear instability and/or negative Ri
 710 values for convective instability due to the overturning of isentropes, which results in critical
 711 level reflection and strong DW events near the surface in the downstream. Thus, most DW cases
 712 with a critical level with small Ri and critical level reflection are in cluster 1, the south high and
 713 north low pattern.



714

715 **Figure 14.** The ratio of downslope windstorm (DW) events generated by wave breaking at
 716 critical levels above $z = 4$ km (a) and 8 km (b). Green, orange, and red bars indicate that Ri near
 717 the critical level are below 1, 0.25, and 0, respectively.

718

719 7 Conclusions

720 Downslope windstorms (DWs) are severe winds generated when a flow across a
 721 mountain is accelerated on the lee side. They are typically generated by hydraulic jumps, partial
 722 reflections of mountain waves, and critical level reflections with wave breaking. DWs often
 723 occur in the springtime and the wintertime in Yeongdong region (YD), located on the lee side of
 724 the Taebaek Mountains (TM) in Korea, and they are frequently responsible for disasters such as
 725 wildfires and low level turbulence. At the PyeongChang 2018 Olympic and Paralympic winter

726 games, there was a DW event that caused structural damage to and the cancellations of some
727 outdoor games such as the ski jump and biathlon on 14–15 Feb 2018. The YD was the main area
728 for the International Collaborative Experiments for the PyeongChang 2018 Olympic and
729 Paralympic winter games (ICE-POP 2018). Previous studies have shown that when DWs
730 associated with wildfires occur in this region, south high and north low synoptic SLP patterns
731 have frequently been observed and accompanied by warm advection and an inversion layer near
732 the top of the mountains (Kim and Chung 2006; Jang and Chun 2010).

733 Here, we used an unsupervised neural network algorithm, a self-organizing map (SOM),
734 to classify synoptic SLP patterns responsible for the DW events found in 41 years of records. We
735 found that the optimal number of clusters is eight, which is where the ECV begins to be saturated
736 and the TE has a local minimum, implying that individual clusters are well separated. Those
737 eight clusters can be categorized into three representative types: 1) the south high and north low
738 pattern, 2) the west high and east low pattern, and 3) the strong low pressure system passing in
739 the northern part of Korea. The monthly distribution in each cluster shows that the occurrence of
740 Type 1 is dominant in the springtime, the occurrence of Type 2 is dominant in the wintertime,
741 and Type 3 occurs in both spring and winter. At the 850 hPa level, near the top of the TM,
742 prevailing southwesterly flow with warm advection can be found in Type 1, while prevailing
743 northwesterly flow with cold advection can be found in Type 2. Cold and warm advection can be
744 found in the back and front of the center of low respectively in Type 3, indicating that the low-
745 pressure system is baroclinic and well-developed.

746 Surface temperature anomalies both on the lee side of the mountain and on the mountain
747 were found to increase in Type 1 but decrease in the other types when the maximum wind speed
748 was measured due to synoptic temperature advection over the Korean Peninsula. Additionally,
749 the surface temperature anomalies were found to be larger on the lee side of the mountain than
750 on the mountain in all clusters, but the difference was found to be the largest in Type 1. This
751 suggests that the adiabatic warming via descending air flow in the downstream of the mountain
752 (i.e., the Föhn effect) is the highest in Type 1, implying that warm and dry air with strong winds
753 can more frequently contribute to the rapid spread of severe wildfires in this area in the
754 springtime (dry season).

755 We investigated how the mesoscale mechanisms responsible for DWs are different under
756 the classified weather patterns. Here, the representative mesoscale generation mechanisms for
757 the DWs are hydraulic jumps, partial reflections of mountain waves, and wave breaking at
758 critical levels. More events explained by hydraulic jump theory were found to be in Type 2 than
759 other types because upstream flows with moderately subcritical Froude number (Fr) and
760 inversion layers were more frequently observed. Meanwhile, we found more events to be
761 generated by partially reflected mountain waves in springtime patterns (Type 1 and cluster 6 in
762 Type 3) than in wintertime patterns (Type 2 and cluster 7 in Type 3) for a wide range of
763 horizontal wavelengths used to calculate the vertical wavenumber, although the partial reflection
764 of mountain waves was found to be related to most DW events in general. In addition, most DW
765 events with critical level reflection and wave breaking in the upper troposphere were found to
766 occur in cluster 1 in Type 1.

767 This study reveals that springtime DW events occur under the south high and north low
768 SLP pattern (Type 1) with relatively more chances of generation mechanisms related to
769 mountain waves such as partial reflection and critical level reflection. This type causes a stronger
770 Föhn effect (i.e., adiabatic warming), resulting in drier and warmer air on the lee side, which is

771 associated with strong wildfires in the YD in the springtime. On the other hand, wintertime DW
772 events were found to occur under the west high and east low SLP pattern (Type 2), which
773 includes cold advection in the lower troposphere that enhances PBL mixing and an inversion
774 layer at the top of the PBL. This provides favorable conditions for hydraulic jumps. Both these
775 two patterns and the strong low pattern in the East Sea of Korea (Type 3) can generate DWs in
776 both spring and winter.

777 For future work, DW events under the different synoptic SLP patterns classified in this
778 study will be investigated in more detail via high resolution numerical model simulation because
779 there are still several local factors such as the channeling effect and drainage flow that may
780 explain extreme winds embedded in the DW events in local areas. Since there would be a
781 limitation in analyzing detailed atmospheric flows solely using the large-scale weather patterns
782 in this study, detailed vertical structures of DWs and propagating mountain waves in concert
783 with local effects by resolved and unresolved topography as well as numerical mesoscale model
784 simulation with a high resolution are required to address these problems, so that we may
785 eventually provide more fine-scale structures of turbulence during DW events in the YD under
786 different regimes. Nevertheless, this study suggests that DWs in the YD in Korea can be
787 classified via objective synoptic SLP patterns using a machine learning algorithm (SOM).
788 Additionally, the types of DWs show inherent differences in the characteristics of background
789 wind and stability, resulting in different contributions to generation mechanisms. This objective
790 classification of DW events in the YD will eventually be very useful in providing baseline
791 information for better predictions and future projections of DW events in this area.

792 **Acknowledgments**

793 This research was supported by the Basic Science Research Program through the National
794 Research Foundation of Korea (NRF), funded by the Ministry of Education. (NRF-
795 2019R111A2A01060035).

796 **Data Availability Statement**

797 The Self-Organizing Map (SOM) toolbox can be download at
798 <http://www.cis.hut.fi/projects/somtoolbox/>. The automated surface observing system (ASOS)
799 data in South Korea are available at the following website (in Korean):
800 <https://data.kma.go.kr/data/grnd/selectAsosRltmList.do?pgmNo=36>. The National Centers for
801 Environmental Prediction–Department of Energy (NCEP–DOE) Reanalysis 2 data can be
802 obtained from <https://psl.noaa.gov/data/gridded/data.ncep.reanalysis2.html>. Fifth-generation
803 ECMWF reanalysis (ERA5) hourly data on pressure levels are available from
804 <https://cds.climate.copernicus.eu/cdsapp#!/dataset/reanalysis-era5-pressure-levels?tab=overview>.

805 **References**

- 806 Abarbanel, H. D., Holm, D. D., Marsden, J. E., & Ratiu, T. (1984). Richardson number criterion
807 for the nonlinear stability of three-dimensional stratified flow. *Physical Review Letters*, 52(26),
808 2352. <https://doi.org/10.1103/PhysRevLett.52.2352>
- 809 Abarbanel, H. D., Holm, D. D., Marsden, J. E., & Ratiu, T. S. (1986). Nonlinear stability
810 analysis of stratified fluid equilibria. *Philosophical Transactions of the Royal Society of London.*
811 *Series A, Mathematical and Physical Sciences*, 318(1543), 349-409.
812 <https://doi.org/10.1098/rsta.1986.0078>

- 813 Cho, Y.-J., Kwon, T.-Y., & Choi, B.-C. (2015). Characteristics of Meteorological Variables in
814 the Leeward Side associated with the Downslope Windstorm over the Yeongdong Region.
815 *Journal of the Korean Earth Science Society*, 36(4), 315-329.
816 <https://doi.org/10.5467/JKESS.2015.36.4.315> (In Korean with English Abstract)
- 817 Cho, Y.-J., Lee, H.-C., Lim, B., & Kim, S.-B. (2019). Classification of Weather Patterns in the
818 East Asia Region using the K-means Clustering Analysis. *Atmosphere*, 29(4), 451-461.
819 <https://doi.org/10.14191/Atmos.2019.29.4.451>
- 820 Clark, T. L., & Peltier, W. R. (1984). Critical level reflection and the resonant growth of
821 nonlinear mountain waves. *Journal of Atmospheric Sciences*, 41(21), 3122-3134.
822 [https://doi.org/10.1175/1520-0469\(1984\)041<3122:CLRATR>2.0.CO;2](https://doi.org/10.1175/1520-0469(1984)041<3122:CLRATR>2.0.CO;2)
- 823 Decker, S. G., & Robinson, D. A. (2011). Unexpected high winds in northern New Jersey: A
824 downslope windstorm in modest topography. *Weather and forecasting*, 26(6), 902-921.
825 <https://doi.org/10.1175/WAF-D-10-05052.1>
- 826 Durran, D. R. (1986). Another look at downslope windstorms. Part I: The development of
827 analogs to supercritical flow in an infinitely deep, continuously stratified fluid. *Journal of*
828 *Atmospheric Sciences*, 43(21), 2527-2543. [https://doi.org/10.1175/1520-](https://doi.org/10.1175/1520-0469(1986)043<2527:ALADWP>2.0.CO;2)
829 [0469\(1986\)043<2527:ALADWP>2.0.CO;2](https://doi.org/10.1175/1520-0469(1986)043<2527:ALADWP>2.0.CO;2)
- 830 Durran, D. R. (1990). Mountain waves and downslope winds. In *Atmospheric processes over*
831 *complex terrain* (pp. 59-81). American Meteorological Society, Boston, MA.
832 https://doi.org/10.1007/978-1-935704-25-6_4
- 833 Glisan, J. M., Gutowski Jr, W. J., Cassano, J. J., Cassano, E. N., & Seefeldt, M. W. (2016).
834 Analysis of WRF extreme daily precipitation over Alaska using self-organizing maps. *Journal of*
835 *Geophysical Research: Atmospheres*, 121(13), 7746-7761.
836 <https://doi.org/10.1002/2016JD024822>
- 837 Hoinka, K. P. (1985). Observation of the airflow over the Alps during a foehn event. *Quarterly*
838 *Journal of the Royal Meteorological Society*, 111(467), 199-224.
839 <https://doi.org/10.1002/qj.49711146709>
- 840 Houghton, D. D., & Kasahara, A. (1968). Nonlinear shallow fluid flow over an isolated ridge.
841 *Communications on Pure and Applied Mathematics*, 21(1), 1-23.
842 <https://doi.org/10.1002/cpa.3160210103>
- 843 Howard, L. N. (1961). Note on a paper of John W. Miles. *Journal of Fluid Mechanics*, 10(4),
844 509-512. <https://doi.org/10.1017/S0022112061000317>
- 845 Jang, W., & Chun, H.-Y. (2008). Severe Downslope Windstorms of Gangneung in the
846 Springtime. *Atmosphere*, 18(3), 207-224. (In Korean with English Abstract)
- 847 Jang, W., & Chun, H.-Y. (2010). A numerical study on severe downslope windstorms occurred
848 on 5 April 2005 at Gangneung and Yangyang, Korea. *Asia-Pacific Journal of Atmospheric*
849 *Sciences*, 46(2), 155-172. <https://doi.org/10.1007/s13143-010-0015-2>
- 850 Jo, E., Park, C., Son, S. W., Roh, J. W., Lee, G. W., & Lee, Y. H. (2020). Classification of
851 localized heavy rainfall events in South Korea. *Asia-Pacific Journal of Atmospheric Sciences*,
852 56(1), 77-88. <https://doi.org/10.1007/s13143-019-00128-7>

- 853 Kim, J., & Paik, K. (2015). Recent recovery of surface wind speed after decadal decrease: a
854 focus on South Korea. *Climate Dynamics*, 45(5), 1699-1712. [10.1007/s00382-015-2546-9](https://doi.org/10.1007/s00382-015-2546-9)
- 855 Kim, J. H., & Chun, H. Y. (2010). A numerical study of clear-air turbulence (CAT) encounters
856 over South Korea on 2 April 2007. *Journal of applied meteorology and climatology*, 49(12),
857 2381-2403. <https://doi.org/10.1175/2010JAMC2449.1>
- 858 Kim, J.-H., & Chung, I.-U. (2006). Study on Mechanisms and Orographic Effect for the
859 Springtime Downslope Windstorm over the Yeongdong Region. *Atmosphere*, 16(2), 67-83. (In
860 Korean with English Abstract)
- 861 Kiviluoto, K. (1996, June). Topology preservation in self-organizing maps. In *Proceedings of*
862 *International Conference on Neural Networks (ICNN'96)* (Vol. 1, pp. 294-299). IEEE.
863 [10.1109/ICNN.1996.548907](https://doi.org/10.1109/ICNN.1996.548907)
- 864 Klemp, J. B., & Lilly, D. R. (1975). The dynamics of wave-induced downslope winds. *Journal of*
865 *Atmospheric Sciences*, 32(2), 320-339. [https://doi.org/10.1175/1520-
866 0469\(1975\)032<0320:TADOWID>2.0.CO;2](https://doi.org/10.1175/1520-0469(1975)032<0320:TADOWID>2.0.CO;2)
- 867 Kohonen, T. (1995). Self-organizing maps.
- 868 Kohonen, T. (2013). Essentials of the self-organizing map. *Neural networks*, 37, 52-65.
869 <https://doi.org/10.1016/j.neunet.2012.09.018>
- 870 Lee, J., Seo, J. M., Baik, J. J., Park, S. B., & Han, B. S. (2020). A Numerical Study of
871 Windstorms in the Lee of the Taebaek Mountains, South Korea: Characteristics and Generation
872 Mechanisms. *Atmosphere*, 11(4), 431. <https://doi.org/10.3390/atmos11040431>
- 873 Lee, J. G., & In, S. R. (2009). A numerical sensitivity experiment of the downslope windstorm
874 over the Yeongdong region in relation to the inversion layer of temperature. *Atmosphere*, 19(4),
875 331-344.
- 876 Lilly, D. K. (1978). A severe downslope windstorm and aircraft turbulence event induced by a
877 mountain wave. *Journal of Atmospheric Sciences*, 35(1), 59-77. [https://doi.org/10.1175/1520-
878 0469\(1978\)035<0059:ASDWAA>2.0.CO;2](https://doi.org/10.1175/1520-0469(1978)035<0059:ASDWAA>2.0.CO;2)
- 879 Lin, Y. L., & Wang, T. A. (1996). Flow regimes and transient dynamics of two-dimensional
880 stratified flow over an isolated mountain ridge. *Journal of the atmospheric sciences*, 53(1), 139-
881 158. [https://doi.org/10.1175/1520-0469\(1996\)053<0139:FRATDO>2.0.CO;2](https://doi.org/10.1175/1520-0469(1996)053<0139:FRATDO>2.0.CO;2)
- 882 Liu, Y., Weisberg, R. H., & Mooers, C. N. (2006). Performance evaluation of the self-organizing
883 map for feature extraction. *Journal of Geophysical Research: Oceans*, 111(C5).
884 <https://doi.org/10.1029/2005JC003117>
- 885 Loikith, P. C., Lintner, B. R., & Sweeney, A. (2017). Characterizing large-scale meteorological
886 patterns and associated temperature and precipitation extremes over the northwestern United
887 States using self-organizing maps. *Journal of Climate*, 30(8), 2829-2847.
888 <https://doi.org/10.1175/JCLI-D-16-0670.1>
- 889 Long, R. R. (1953). Some aspects of the flow of stratified fluids: I. A theoretical investigation.
890 *Tellus*, 5(1), 42-58. <https://doi.org/10.3402/tellusa.v5i1.8563>
- 891 Long, R. R. (1954). Some aspects of the flow of stratified fluids: II. Experiments with a two-
892 fluid system. *Tellus*, 6(2), 97-115. <https://doi.org/10.1111/j.2153-3490.1954.tb01100.x>

- 893 Miles, J. W. (1961). On the stability of heterogeneous shear flows. *Journal of Fluid Mechanics*,
894 10(4), 496-508. <https://doi.org/10.1017/S0022112061000305>
- 895 Miles, J. (1986). Richardson's criterion for the stability of stratified shear flow. *The Physics of*
896 *fluids*, 29(10), 3470-3471. <https://doi.org/10.1063/1.865812>
- 897 Neal, R., Fereday, D., Crocker, R., & Comer, R. E. (2016). A flexible approach to defining
898 weather patterns and their application in weather forecasting over Europe. *Meteorological*
899 *Applications*, 23(3), 389-400. <https://doi.org/10.1002/met.1563>
- 900 Nguyen-Le, D., & Yamada, T. J. (2019). Using weather pattern recognition to classify and
901 predict summertime heavy rainfall occurrence over the Upper Nan river basin, northwestern
902 Thailand. *Weather and Forecasting*, 34(2), 345-360. <https://doi.org/10.1175/WAF-D-18-0122.1>
- 903 Ohba, M., Kadokura, S., Yoshida, Y., Nohara, D., & Toyoda, Y. (2015). Anomalous weather
904 patterns in relation to heavy precipitation events in Japan during the Baiu season. *Journal of*
905 *Hydrometeorology*, 16(2), 688-701. <https://doi.org/10.1175/JHM-D-14-0124.1>
- 906 Philipp, A., Della-Marta, P. M., Jacobeit, J., Fereday, D. R., Jones, P. D., Moberg, A., &
907 Wanner, H. (2007). Long-term variability of daily North Atlantic–European pressure patterns
908 since 1850 classified by simulated annealing clustering. *Journal of Climate*, 20(16), 4065-4095.
909 <https://doi.org/10.1175/JCLI4175.1>
- 910 Scorer, R. S. (1949). Theory of waves in the lee of mountains. *Quarterly Journal of the Royal*
911 *Meteorological Society*, 75(323), 41-56. <https://doi.org/10.1002/qj.49707532308>
- 912 Seluchi, M. E., Norte, F. A., Satyamurty, P., & Chou, S. C. (2003). Analysis of three situations
913 of the foehn effect over the Andes (zonda wind) using the Eta–CPTEC regional model. *Weather*
914 *and forecasting*, 18(3), 481-501. [https://doi.org/10.1175/1520-0434\(2003\)18<481:AOTSOT>2.0.CO;2](https://doi.org/10.1175/1520-0434(2003)18<481:AOTSOT>2.0.CO;2)
- 915
- 916 Vautard, R., Cattiaux, J., Yiou, P., Thépaut, J. N., & Ciais, P. (2010). Northern Hemisphere
917 atmospheric stilling partly attributed to an increase in surface roughness. *Nature geoscience*,
918 3(11), 756-761. 10.1038/NGEO979
- 919 Vosper, S. B. (2004). Inversion effects on mountain lee waves. *Quarterly Journal of the Royal*
920 *Meteorological Society: A journal of the atmospheric sciences, applied meteorology and physical*
921 *oceanography*, 130(600), 1723-1748. <https://doi.org/10.1256/qj.03.63>
- 922 Wang, T. A., & Lin, Y. L. (2000). Effects of shear and sharp gradients in static stability on two-
923 dimensional flow over an isolated mountain ridge. *Meteorology and Atmospheric Physics*, 75(1),
924 69-99. <https://doi.org/10.1007/s007030070017>
- 925 Zeng, Z., Ziegler, A. D., Searchinger, T., Yang, L., Chen, A., Ju, K., ... & Wood, E. F. (2019). A
926 reversal in global terrestrial stilling and its implications for wind energy production. *Nature*
927 *Climate Change*, 9(12), 979-985. <https://doi.org/10.1038/s41558-019-0622-6>
- 928